NATIONAL ENERGY TECHNOLOGY LABORATORY

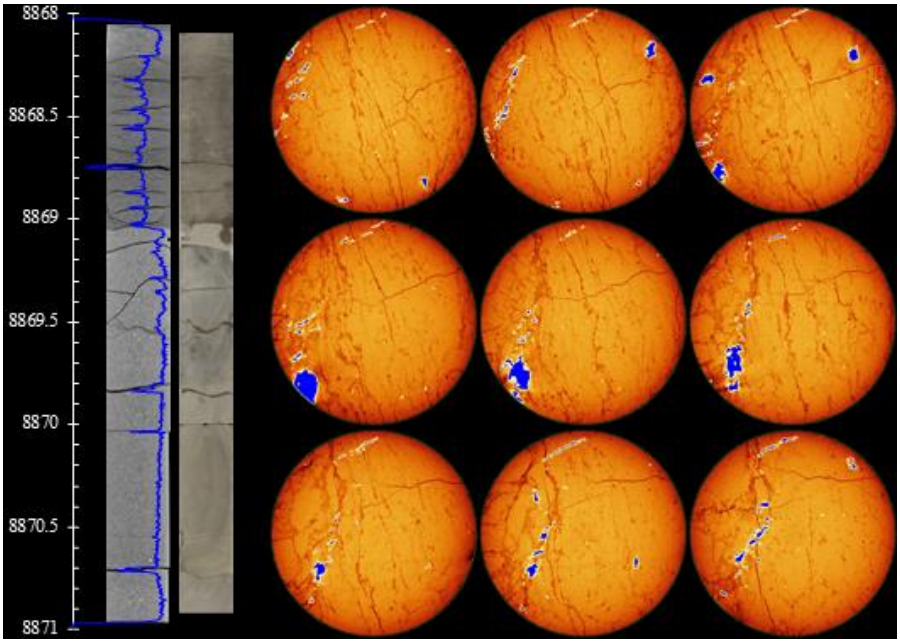

Computed Tomography Scanning and Geophysical Measurements of the Smackover Formation from the Roberson 18-19 Core

20 September 2022

U.S. DEPARTMENT OF ENERGY | NATIONAL ENERGY TECHNOLOGY LABORATORY

Office of Fossil Energy and Carbon Management

DOE/NETL-2022/3735

Disclaimer

This project was funded by the United States Department of Energy, National Energy Technology Laboratory, in part, through a site support contract.

Cover Illustration: Mean computed tomography number (CTN) profile superimposed onto CT core image next to 1/3 slabbed core (left) and micro CT image montage (right) of Roberson 18-19, 1 in. sub-core at 9,093.6 ft with false coloring to highlight the distribution of pyrite (blue) and fractures (brown) in the limestone matrix (orange).

Suggested Citation: Mitchell, N.; Paronish, T.; Schmidt, R.; Moore, J.; Crandall, D.; Brown, S.; Jarvis, K.; Dotson, B. *Computed Tomography Scanning and Geophysical Measurements of the Smackover Formation from the Roberson 18-19 Core;* DOE.NETL-2022.3735; NETL Technical Report Series; U.S. Department of Energy, National Energy Technology Laboratory: Morgantown, WV, 2022; p 68. DOI: 10.2172/1887969.

An electronic version of this report can be found at:

https://netl.doe.gov/energy-analysis/search

https://edx.netl.doe.gov/ucr

The data in this report can be accessed from NETL's Energy Data eXchange (EDX) online system (https://edx.netl.doe.gov) using the following link:

https://edx.netl.doe.gov/dataset/roberson-smackover

Computed Tomography Scanning and Geophysical Measurements of the Smackover Formation from the Roberson 18-19 Core

Natalie Mitchell[1,2], Thomas Paronish[1,2], Rhiannon Schmitt[1,3], Johnathan Moore[1,2], Dustin Crandall[1], Sarah Brown[1,2], Karl Jarvis[1,2], Ben Dotson[4]

[1]National Energy Technology Laboratory, 3610 Collins Ferry Road, Morgantown, WV 26505

[2]NETL Support Contractor, 3610 Collins Ferry Road, Morgantown, WV 26505

[3]Oak Ridge Institute for Science and Education (ORISE), 3610 Collins Ferry Road, Morgantown, WV 26505

[4]Southwestern Energy, 1000 Energy Drive, Spring, TX 77389

DOE/NETL-2022/3735

20 September 2022

NETL Contacts:

Dustin Crandall, Principal Investigator

Christina Lopano and Eilis Rosenbaum, Technical Portfolio Leads

Bryan Morreale, Associate Laboratory Director for Research & Innovation, Research & Innovation Center

This page intentionally left blank.

Table of Contents

List of Figures

List of Figures (cont.)

List of Tables

Acronyms, Abbreviations, and Symbols

Term	Description
2D	Two-dimensional
3D	Three-dimensional
CT	Computed tomography
CTN	CT number
DOE	U.S. Department of Energy
EDX	NETL's Energy Data eXchange
H	External magnetic field
HU	Hounsfield Units
J	Magnetic response (per unit volume)
k	Volume susceptibility
MSCL	Multi-Sensor Core Logger
NETL	National Energy Technology Laboratory
ρ_B	Density
XRF	X-ray fluorescence

Acknowledgments

This work was completed at the National Energy Technology Laboratory (NETL) with support from U.S. Department of Energy's (DOE) Office of Resource Sustainability. The authors wish to acknowledge Bryan Morreale, Christina Lopano, Eilis Rosenbaum, Dustin McIntyre, and Alexandra Hakala for their support through NETL Research & Innovation Center. In addition, the authors wish to acknowledge John Wimer, (NETL Science & Technology Strategic Plans & Programs) and David Alleman (DOE Office of Resource Sustainability) for programmatic guidance, direction, and support.

The authors would like to thank Bryan Tennant and Scott Workman for data collection and technical support. Thank you to Southwestern Energy Production Company for allowing us to work with this core. This research was supported by an appointment from the NETL Research Participation Program, sponsored by the U.S. DOE and administered by the Oak Ridge Institute for Science and Education (ORISE).

ABSTRACT

The computed tomography (CT) facilities and the Multi-Sensor Core Logger (MSCL) at the U.S. Department of Energy's (DOE) National Energy Technology Laboratory (NETL) site in Morgantown, West Virginia, were used to characterize the Upper Jurassic (Oxfordian) Smackover limestone in the Roberson 18-19 1-15H core retrieved from the Atlanta Field, Columbia County, Arkansas. The 365.68-ft long Roberson core came from a vertical well at depths 8,802 ft to 9,169.60 ft, drilled by Southwestern Energy targeting the Smackover Formation as a potential unconventional oil reservoir.

The primary impetus of this work was to non-destructively characterize core from the Smackover Formation that was acquired through a core exchange with Southwestern Energy. The Smackover Formation is an unconventional limestone play in southern Arkansas. This report and the associated scans provide detailed datasets not typically made publicly available from unconventional limestone for analysis. The resultant datasets are presented in this report and can be accessed from NETL's Energy Data eXchange (EDX) online system using the following link: https://edx.netl.doe.gov/dataset/roberson-smackover.

All equipment and techniques used were non-destructive, enabling future examinations and analyses to be performed on these cores. None of the equipment used was suitable for direct visualization of the tight limestone pore space, although fractures and discontinuities were detectable with the methods tested. Coarse resolution CT imagery with the NETL medical CT scanner was performed on the entire core. Qualitative analysis of the medical CT images, coupled with X-ray fluorescence, P-wave, and magnetic susceptibility measurements from the MSCL were useful in identifying zones of interest for more detailed analysis as well as fractured zones. The ability to quickly identify key areas for more detailed study with higher resolution will save time and resources in future studies. The combination of methods used provided a multi-scale analysis of this core and provided both a macro and micro description of the core that is relevant for many subsurface energy related examinations that have traditionally been performed at NETL.

1. INTRODUCTION

1.1 STUDY AREA

The Atlanta Field in Columbia County, Arkansas, is one of many fields that produce oil from the Upper Jurassic (Oxfordian) Smackover Formation, all of which share similar reservoir properties (Riggs, 1949). The geographic coordinates of the Roberson 18-19 well in the Atlanta Field are latitude 33.16401801, longitude -93.05874627, and the field encompasses Section 15 Township 18S, and Range 19W (Figure 1). The Atlanta Field is located on an east-west trending anticline approximately 6 miles long and approximately 0.5 to 1-mile wide. The Roberson 18-19 well (API 03-027-118430000) was spudded on September 1, 2011, by Southwestern Energy where the targeted reservoir was the Lower Smackover Formation, informally called the Brown Dense. The Roberson core is 365.68 ft long and was retrieved from depths 8,802 ft to 9,169.60 ft (Table 1).

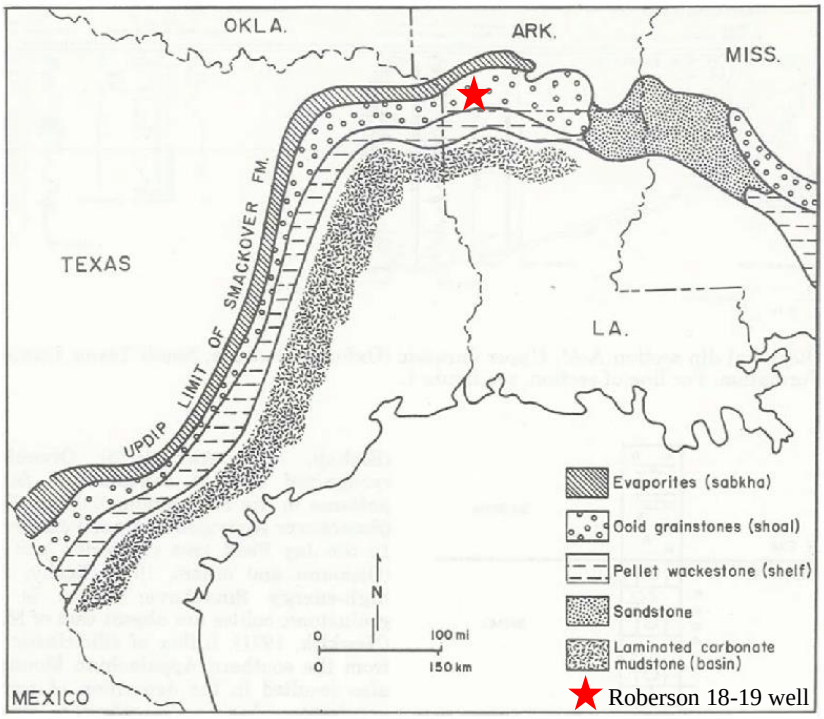

Figure 1: Location of the Roberson 18-19 well in Arkansas and regional map of the Smackover lithofacies belts in the U.S. Gulf Coast Basin (modified from Handford and Baria (2007), Ahr (1973), and Bishop (1986)).

The Upper Jurassic Smackover Formation (154-159 Ma) is part of the Louark Group (150-161 Ma), which consists of the underlying Norphlet Formation and/or Louann salts (159-175 Ma), and the overlying Buckner Anhydrite Member of the Haynesville Formation (150-154 Ma) (Figure 2). According to Riggs (1949), the Cotton Valley group (150-137 Ma), which is also Upper Jurassic in age, rests directly on the Smackover limestone in the Atlanta Field. In the southwestern corner of Arkansas, the Smackover Formation is greater than 1,200-ft thick, but thins updip towards the northern margin of its present extent due to erosion during post Buckner times (Bruce, 1944). Therefore, rocks of Jurassic age do not outcrop in the Gulf Coastal Plain, but underlie eastern Texas, southern Arkansas, Louisiana, central and southern Mississippi, and

southwestern Alabama (Figure 1). Upper Jurassic rocks are found only in the subsurface at depths ranging from 1,000–3,000 ft along their northern limit in southern Arkansas and northeastern Texas to 12,000 ft in northern Louisiana and eastern Texas, and greater depths in central Louisiana and southeastern Texas (Dickinson, 1968).

The Smackover Formation is divided into three informal sub-units: an upper Reynolds Member composed of clean, ooidal grainstone; the Middle Smackover composed of brown, dense, laminated, pelletal, lime-mudstone and fossiliferous lime-wackestone; and the lower Brown Dense unit comprised of dark-brown, fine-grained, laminated, argillaceous, lime-mud sequence (Dickinson, 1968; Moore and Druckman, 1981). Traditional sub-division of the limestone into an upper and lower member are described as transitional into each other and has lateral variation in lithology (Riggs, 1949). Based on the well log, the Roberson 18-19 transects the middle and lower Smackover, which are further described herein (Figure 2).

Evolution of the Gulf of Mexico is linked to deposition of the Late Jurassic Smackover Formation. During the Late Triassic-Early Jurassic, North America separated from Africa-South America forming half-grabens bounded by listric normal faults, widespread doming, and rift basins that were eventually infilled by red-bed sedimentary sequences of the Eagle Mills Formation (Salvador, 1987,1991a). Crustal attenuation and transitional crust formation during Middle Jurassic rifting developed a series of separate arches/uplifts and subsiding basins, where latter isolated basins became filled with thick sequences of evaporite (Mancini et al., 2006). A regional marine transgression related to crustal cooling and subsidence followed during Late Jurassic sea-floor spreading and oceanic crust formation (Sawyer et al., 1991). Early Cretaceous saw continued subsidence, ramping up of a carbonate platform, and deposition of shallow water to deep-water sedimentary rocks along the basin margin. Evolution of the Gulf Coast region ended during the Late Cretaceous, where prominent igneous activity produced global sea-level fall, and shallow Cretaceous platform margin exposure as defined by an unconformity rimming the Gulf (Salvador, 1991b).

SYSTEM	SERIES	GROUP	AGE (Ma)	FORMATION
Jurassic	Upper Jurassic	Cotton Valley	150-137	Schuler
				Bossier
		Louark	154-150	Haynesville (Buckner Member)
			159-154	Smackover
			161-159	Norphlet
	Middle Jurassic		175-163	Louann Salt
			176-175	Werner
Triassic	Late Triassic		210-195	Eagle Mills

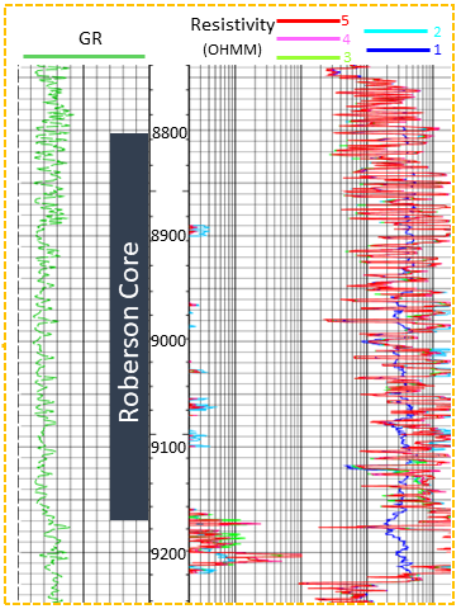

Figure 2: Stratigraphic column of Late Triassic to Late Jurassic Formations of the Northern U.S. Gulf Coast and gamma ray and resistivity well logs with the approximate location of the core from 8,802 to 9,169.60 ft (modified from Arkansas Geological Survey (2022)).

1.2 CORE DESCRIPTION

Four cored sections were retrieved from the Roberson 18-19 well (Table 1). Based on core observation along with gamma ray and medium/deep induction well logs, the Roberson 18-19 core contains the informal lower member of the Smackover Formation from depths of 8,802.0 to 9,169.60 ft. (Figure 2). The core is a burrowed, grey fossiliferous packstone and brown wackestone/mudstone with well-defined grey and black basal lamination.

Table 1 Core Box Distribution of the Roberson 18-19 Core

Core Box	Number of Boxes	Depth Range (ft)
Core 1	9	8,802–8,886
Core 2	10	8,889–8,982
Core 3	10	8,982–9,075
Core 4	10	9,075–9,170

1.3 CORE 1 PHOTOGRAPHS

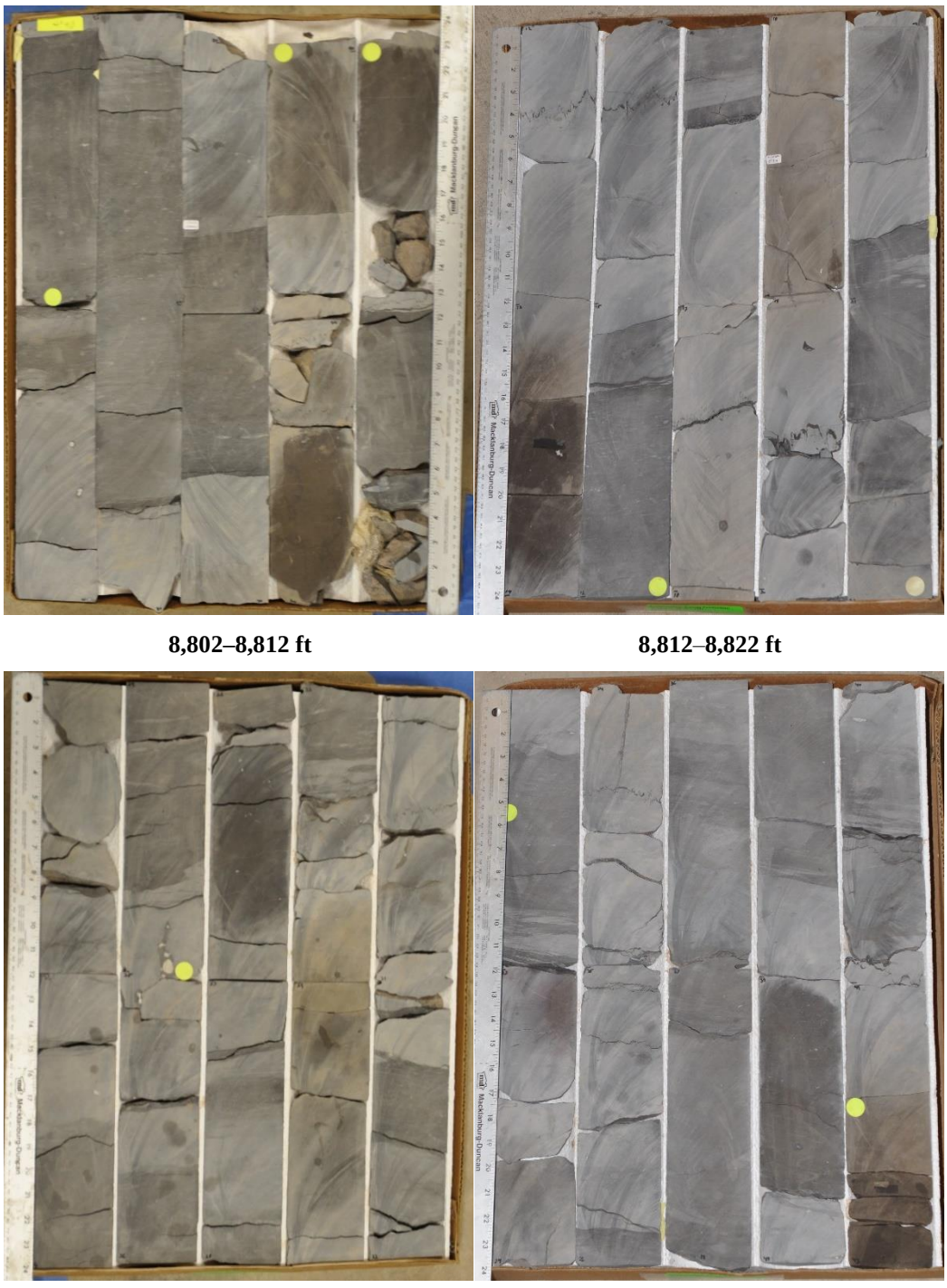

8,802–8,812 ft **8,812–8,822 ft**

8,822–8,832 ft **8,832–8,842 ft**

Figure 3: Photograph of Roberson 18-19 slabbed core from 8,802 to 8,842 ft.

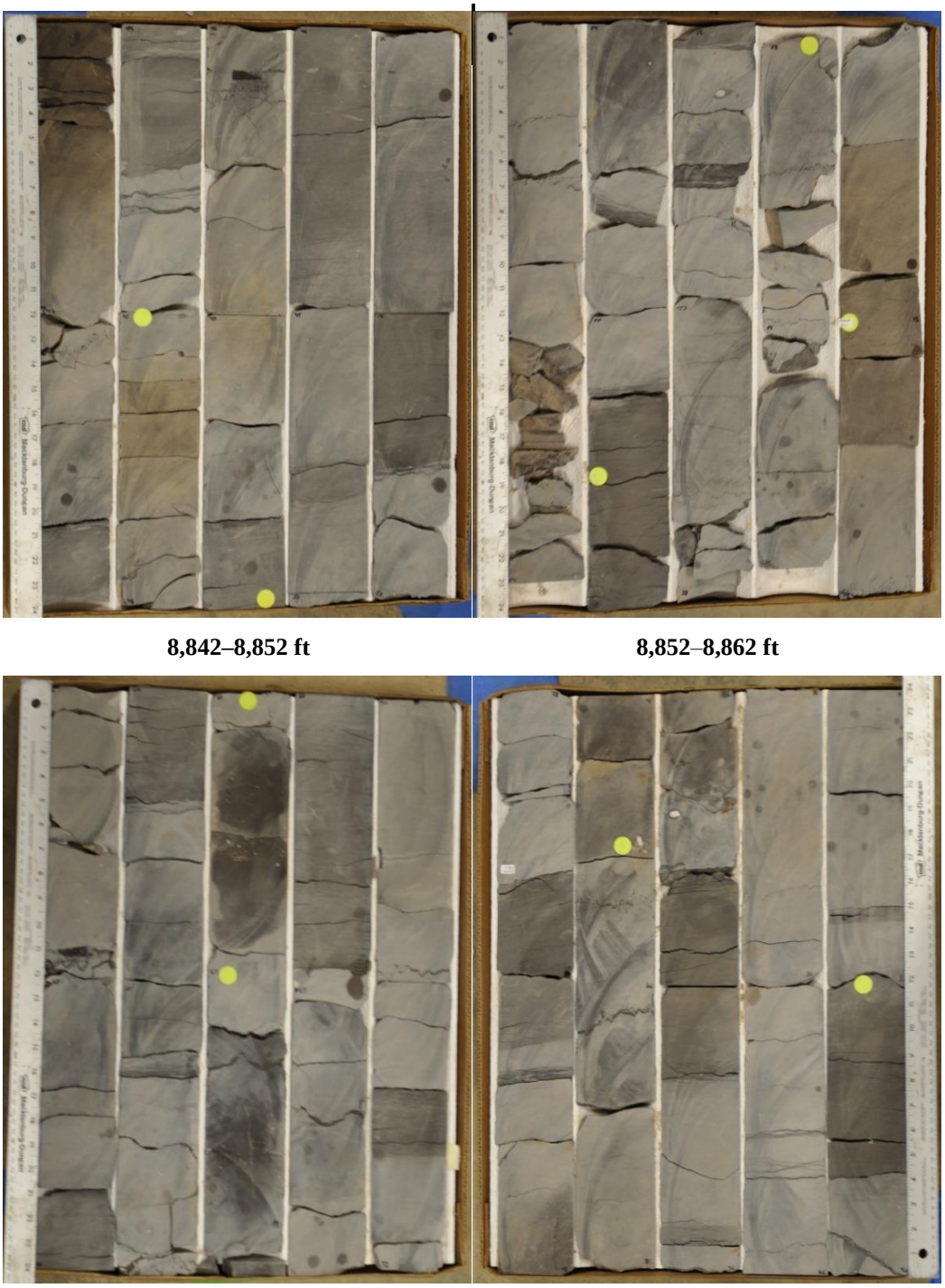

8,842–8,852 ft **8,852–8,862 ft**

8,862–8,872 ft **8,872–8,882 ft**

Figure 4: Photograph of Roberson 18-19 slabbed core from 8,842 to 8,882 ft.

8,882–8,886.35 ft

Figure 5: Photograph of Roberson 18-19 slabbed core from 8,882 to 8,886.35 ft.

1.4 CORE 2 PHOTOGRAPHS

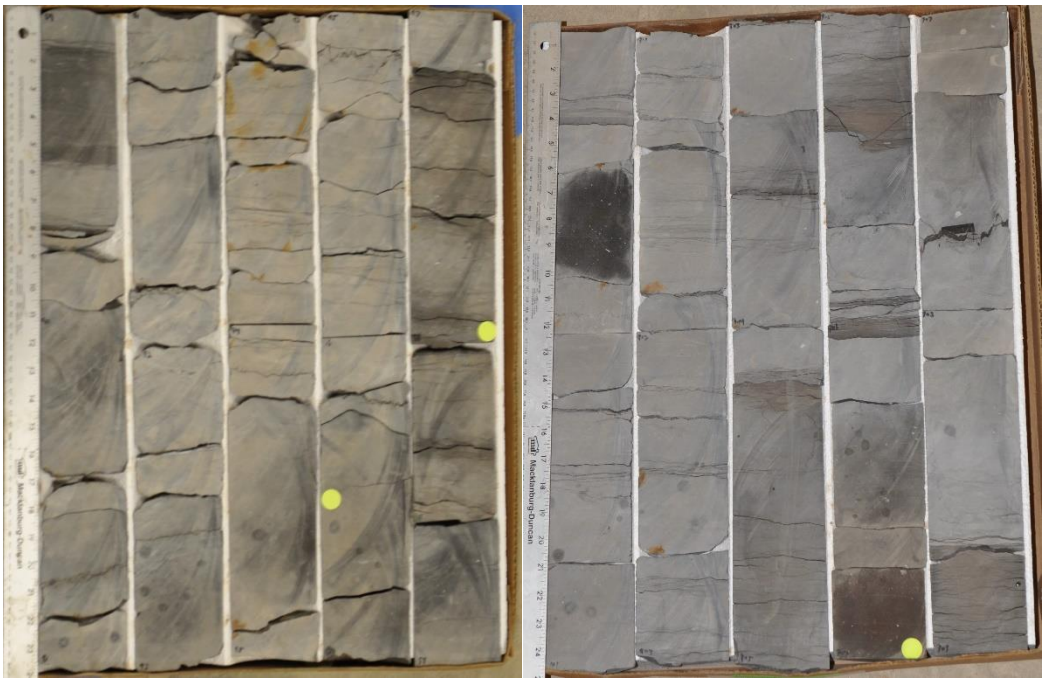

8,889–8,899 ft **8,899–8,909 ft**

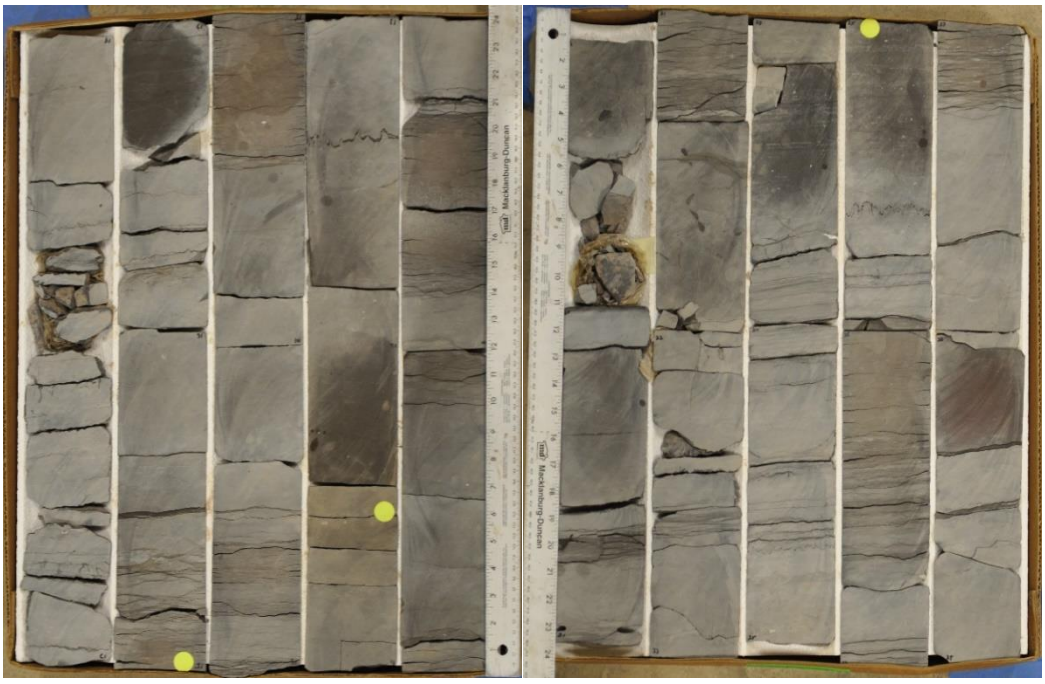

8,909–8,919 ft **8,919–8,929 ft**

Figure 6: Photograph of Roberson 18-19 slabbed core from 8,889 to 8,929 ft.

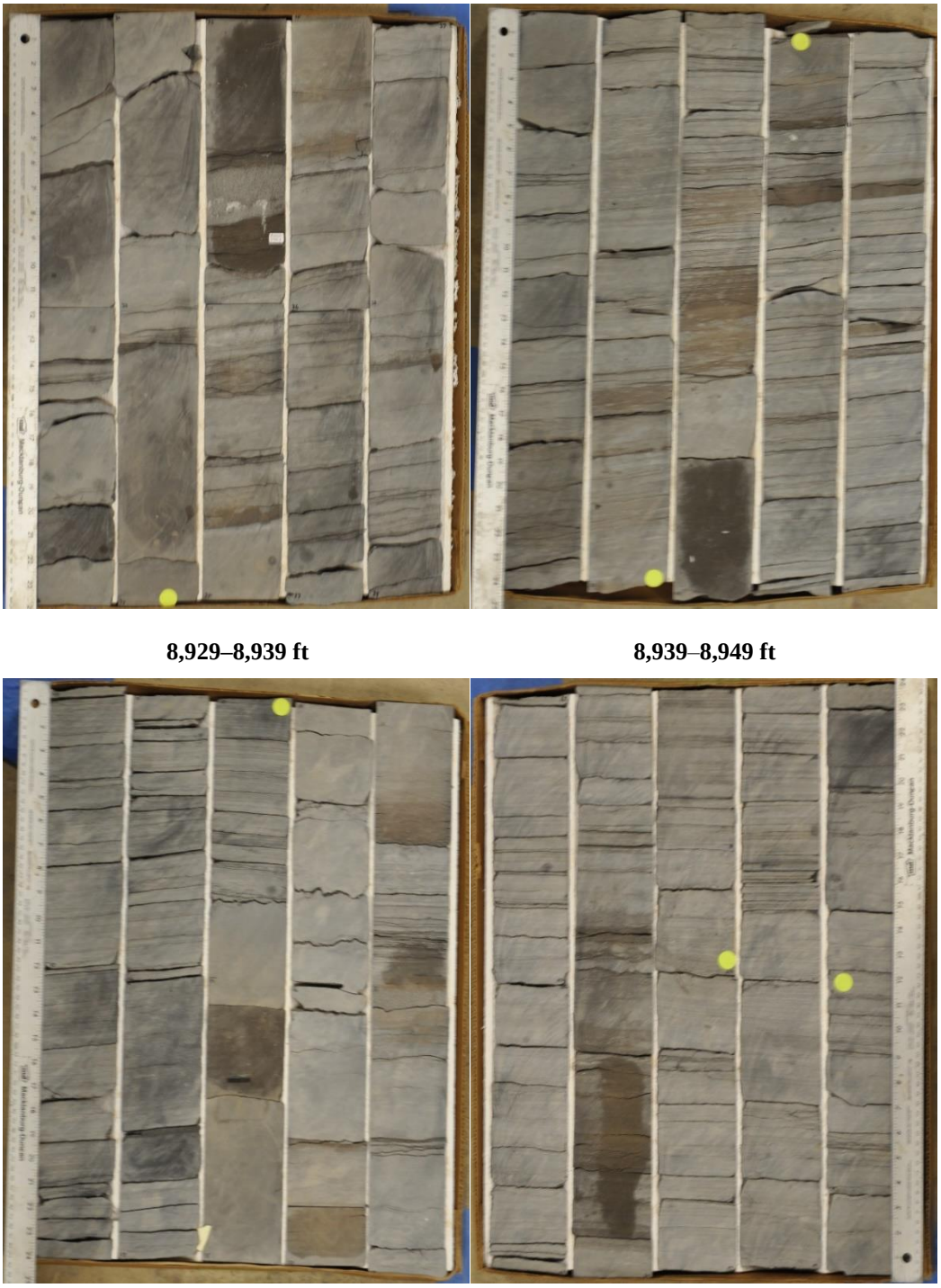

8,929–8,939 ft **8,939–8,949 ft**

8,949–8,959 ft **8,959–8,969 ft**

Figure 7: Photograph of Roberson 18-19 slabbed core from 8,929 to 8,969 ft.

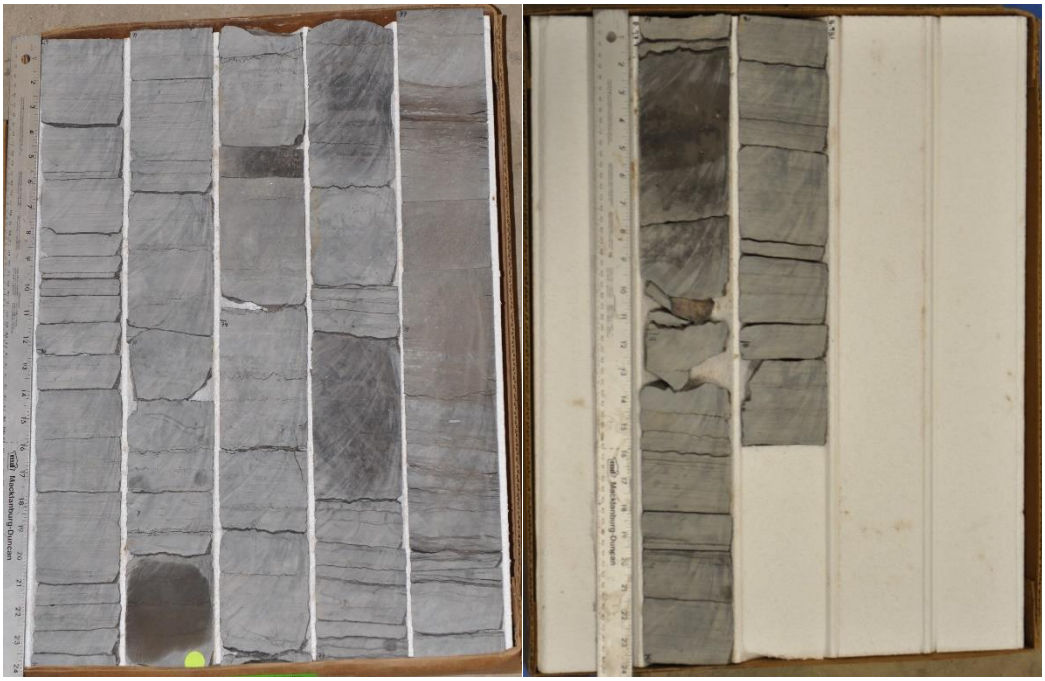

8,969–8,979 ft **8,979–8,982 ft**

Figure 8: Photograph of Roberson 18-19 slabbed core from 8,969 to 8,982 ft.

1.5 CORE 3 PHOTOGRAPHS

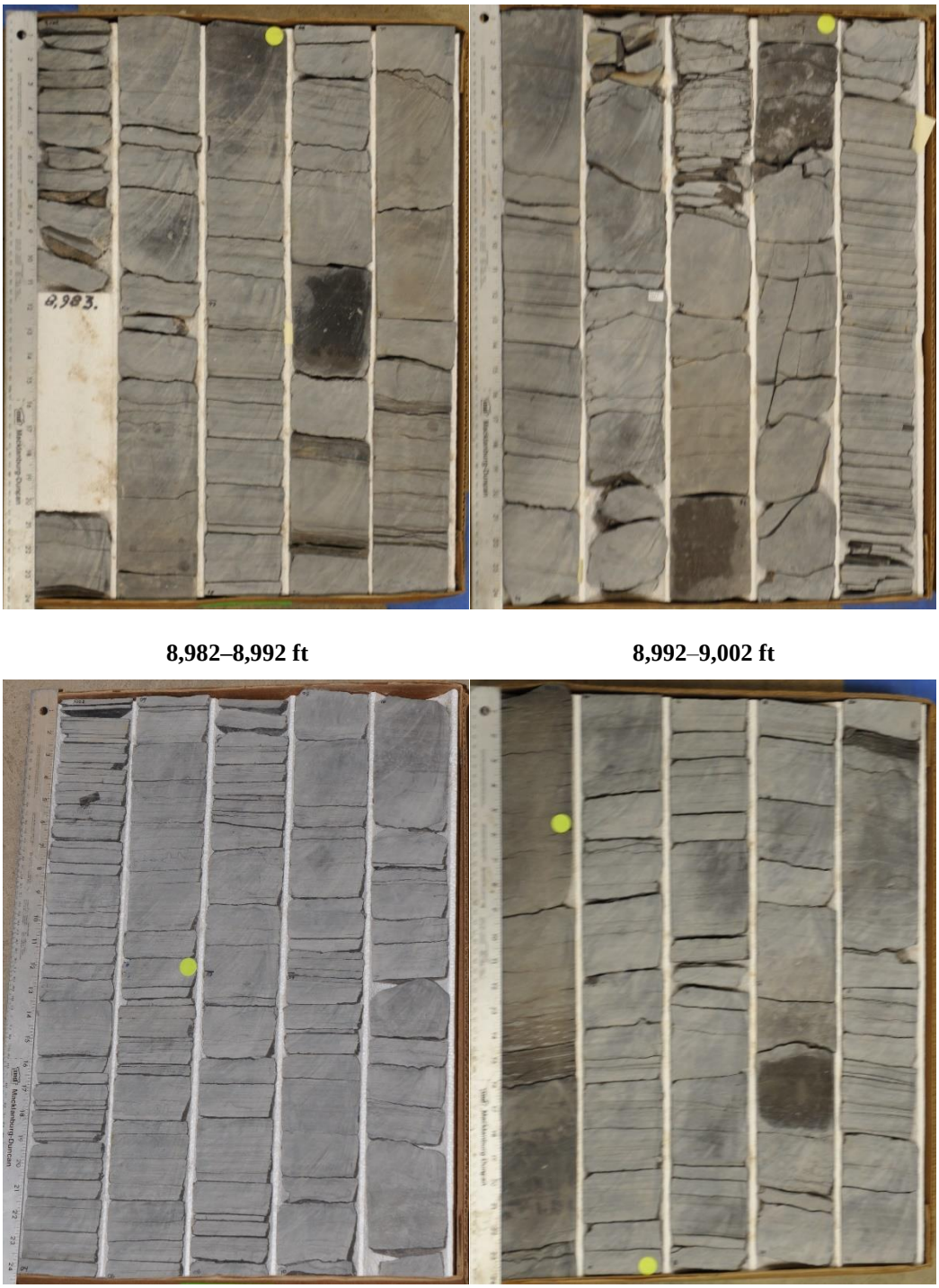

8,982–8,992 ft **8,992–9,002 ft**

9,002–9,012 ft **9,012–9,022 ft**

Figure 9: Photograph of Roberson 18-19 slabbed core from 8,982 to 9,022 ft.

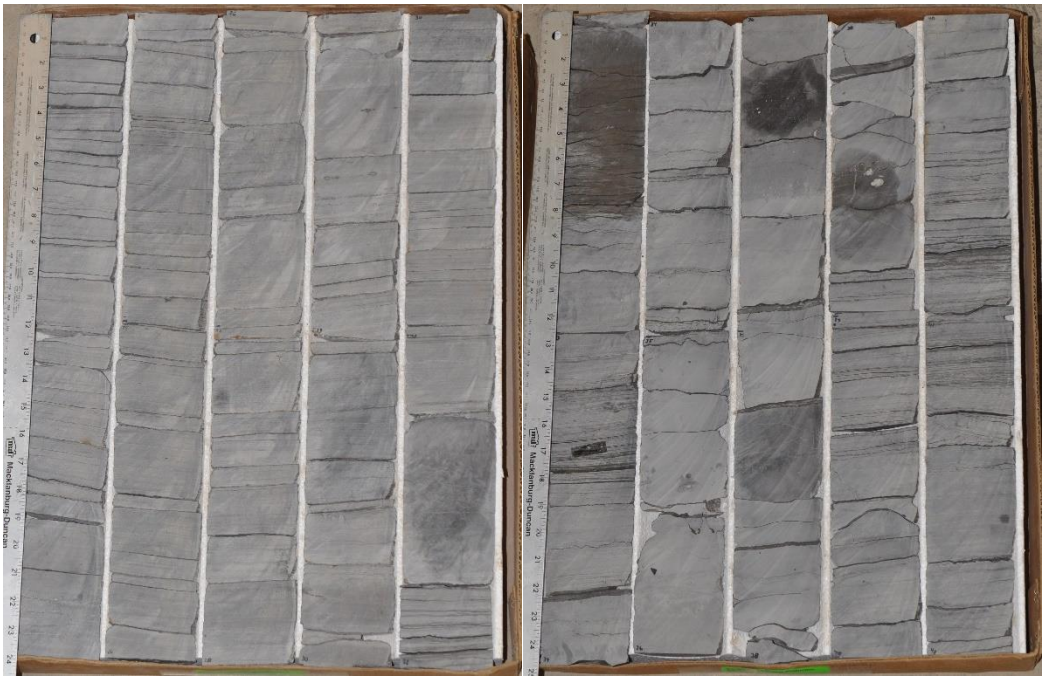

9,022–9,032 ft **9,032–9,042 ft**

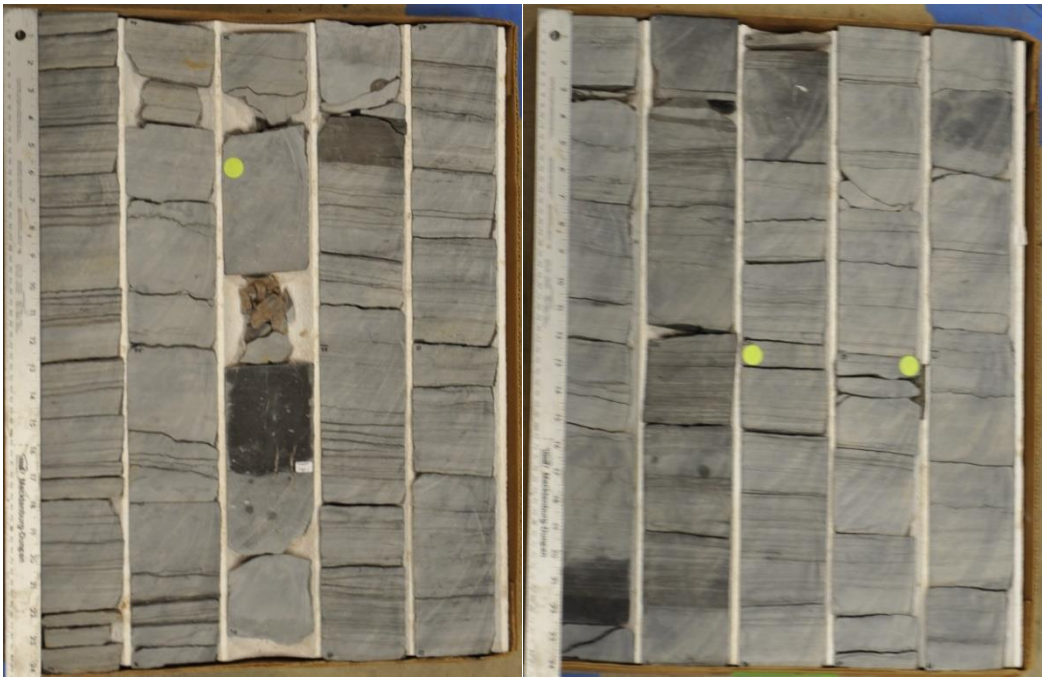

9,042–9,052 ft **9,052–9,062 ft**

Figure 10: Photographs of Roberson 18-19 slabbed core from 9,022 to 9,062 ft.

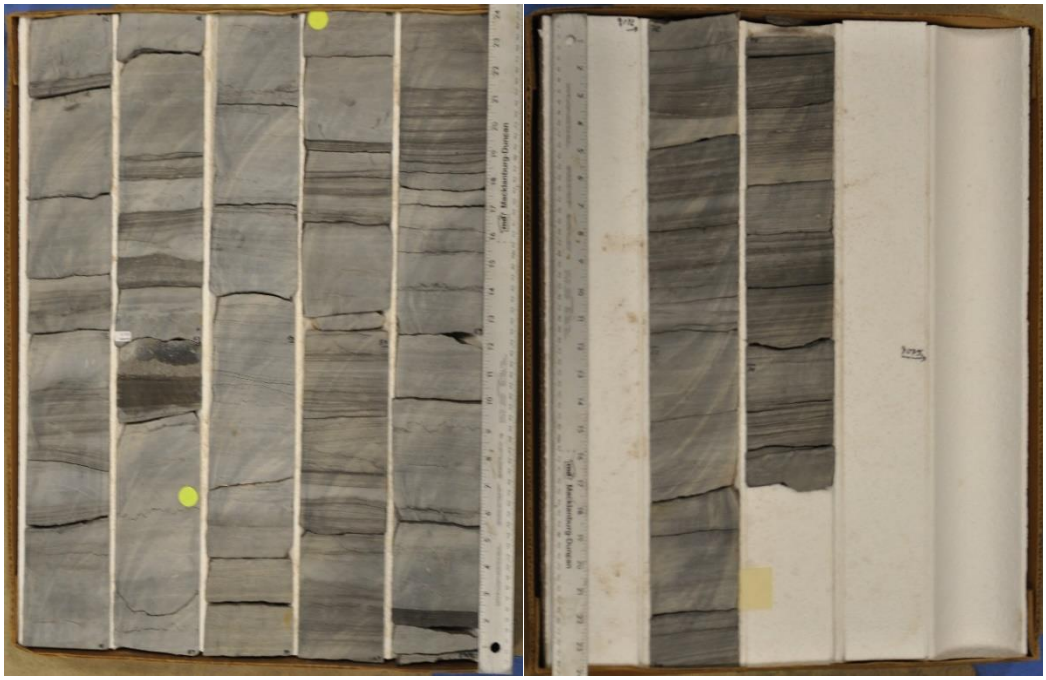

9,062–9,072 ft **9,072–9,075 ft**

Figure 11: Photograph of Roberson 18-19 slabbed core from 9,062 to 9,075 ft.

1.6 CORE 4 PHOTOGRAPHS

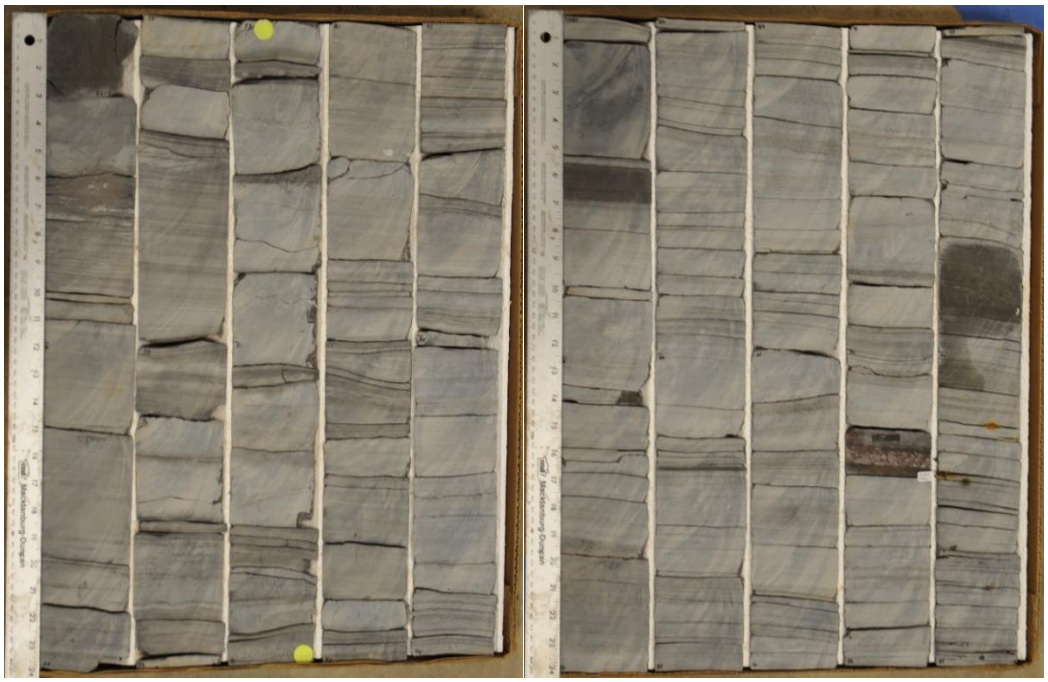

9,075–9,085 ft **9,085–9,095** ft

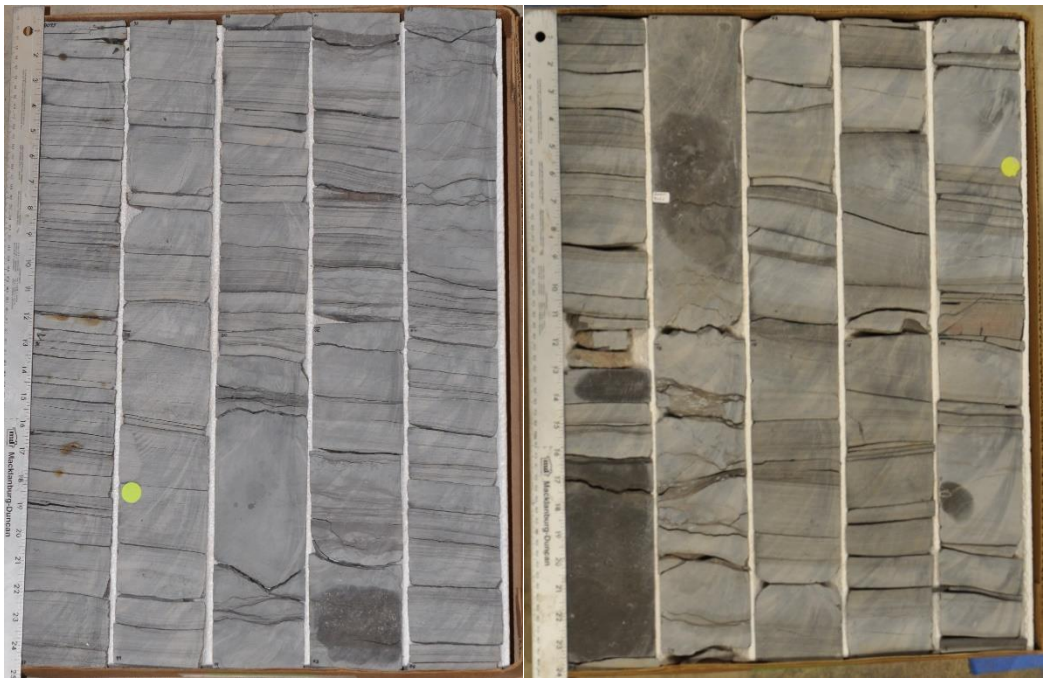

9,095–9,105 ft **9,105–9,115 ft**

Figure 12: Photograph of Roberson 18-19 slabbed core from 9,075 to 9,115 ft.

9,115–9,125 ft **9,125–9,135 ft**

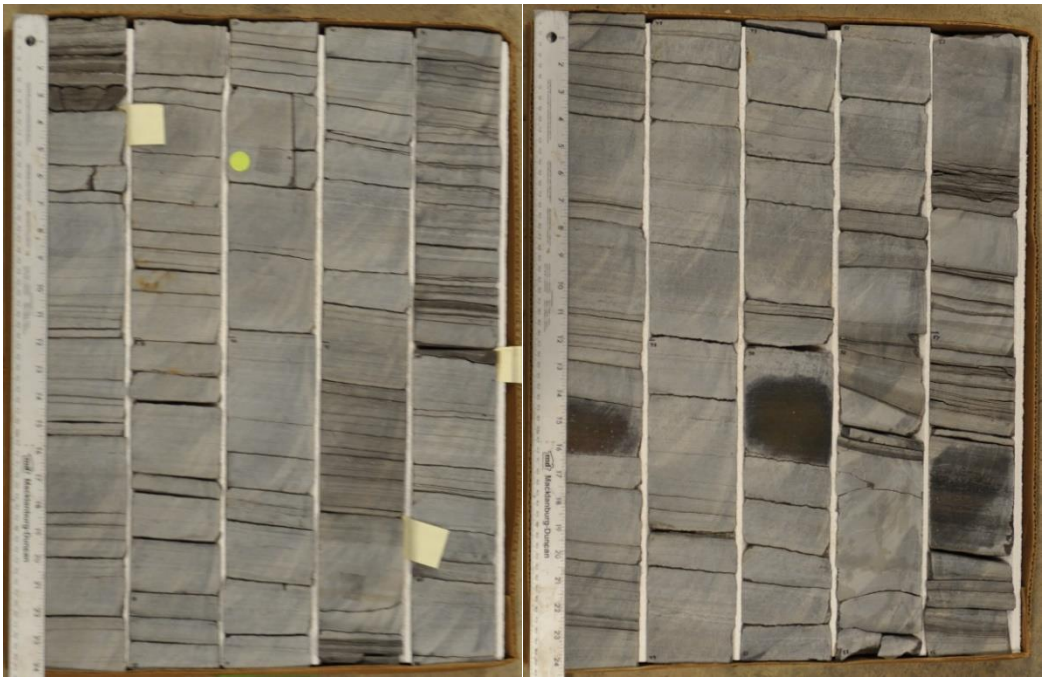

9,135–9,145 ft **9,145–9,155 ft**

Figure 13: Photograph of Roberson 18-19 slabbed core from 9,115 to 9,155 ft.

9,155–9,165 ft **9,165–9,169.60 ft**

Figure 14: Photograph of Roberson 18-19 slabbed core from 9,155 to 9,169.60 ft.

2. DATA ACQUISITION AND METHODOLOGY

The 2/3rd slabbed core was evaluated using computed tomography (CT) scanning and traditional core logging.

2.1 CORE LOGGING

Geophysical measurements of core thickness deviation, P-wave travel time, magnetic susceptibility, and attenuated gamma counts can be obtained with a Geotek® Multi-Sensor Core Logging (MSCL, Figure 15) system on a competent core. For the 2/3rd slabbed core that was scanned as part of this analysis, the P-wave velocity, magnetic susceptibility, and gamma density were measured and reported. Additionally, the system was used to measure bulk elemental chemistry with a built-in, portable X-ray fluorescence (XRF) spectrometer. For a full description of the MSCL capabilities at the National Energy Technology Laboratory (NETL), please see Crandall et al. (2017).

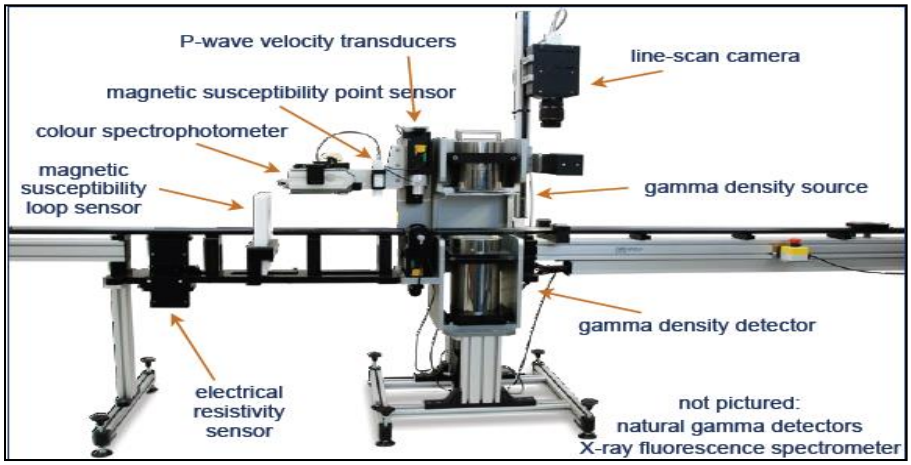

Figure 15: Representation of generalized MSCL with all attached instruments. From Geotek Ltd., Geotek Multi-Sensor Core Logger Flyer, Daventry, UK (2009).

2.1.1 Magnetic Susceptibility

Magnetic susceptibility is a measure of the degree of magnetization in a sample. The sample is exposed to an external magnetic field and magnetic susceptibility is the measured magnetic response to that field:

$$J = kH$$

Where, J is the magnetic response (per unit volume), k is volume susceptibility, and H is an external magnetic field. The measurement unit is dimensionless (abbreviated simply as SI).

All materials have magnetic susceptibility. Positive values of magnetic susceptibility indicate that materials are paramagnetic and occur in rocks that consist of the majority ferromagnetic,

ferrimagnetic, or antimagnetic (iron bearing) materials. Whereas, negative values of magnetic susceptibility indicate that materials are diamagnetic and occur in rocks dominated by non-iron material (i.e., calcite or quartz). Table 2 lists examples of common magnetic susceptibility ranges (Hunts et al., 1995).

Magnetic susceptibility was measured using the Bartington point sensor, where a 1-cm diameter, low-intensity (8.0 A/m RMS) non-sensitive, alternating magnetic field (2 kHz) was generated for 10 s. To minimize any potential drift in the oscillating field, the point sensor was zeroed at the beginning and end of the sample, as well as, after every fifth measurement. The point sensor, due to the small field, was limited in whole core measurements and additionally was temperature dependent (Geotek Ltd. Multi-Sensor Core Logger Manual, Version 05-10; Geotek Ltd., 2010).

Table 2: Magnetic Susceptibility Values for Common Minerals (Hunts et al., 1995)

Mineral	x (*10^{-6}) SI
Water	9
Calcite	-7.5 to -39
Halite, Gypsum	-10 to -60
Shale	63 to 18,600
Illite, Montmorillonite	330 to 410
Pyrite	5 to 3,500
Chalcopyrite	23 to 400
Hematite	500 to 40,000
Magnetite	1,000,000 to 5,700,000

2.1.2 P-wave Velocity

P-wave velocity measurements were performed to measure the acoustic impedance of a geologic sample with compressional waves. Acoustic impedance is a measure of how well a material transmits vibrations, which is directly proportional to density and/or material consolidation. An example of a material that has a high acoustic impedance would be air, with a wave speed of 330 m/s, whereas granite would have low acoustic impedance, with a wave speed of >5,000 m/s. These measurements can be proxies for seismic reflection coefficients and can be translated to field use when doing seismic surveys.

The software associated with the MSCL measured the travel time of the pulse with a resolution of 50 ns. The absolute accuracy of the instrument measurements is $\pm$ 3 m/s with a resolution of 1.5 m/s (Geotek Ltd. Multi-Sensor Core Logger Manual, Version 05-10; Geotek Ltd., 2010).

2.1.3 XRF Spectrometry

In addition to the geophysical measurements, a portable handheld Innov-X® X-Ray Fluorescence Spectrometer was used to measure relative elemental abundances of aggregated “light elements” up to and including sodium, and also various heavy elements which were measured individually

(Figure 16). Elemental abundances are reported relative to the total elemental composition, i.e., out of 100% weight.

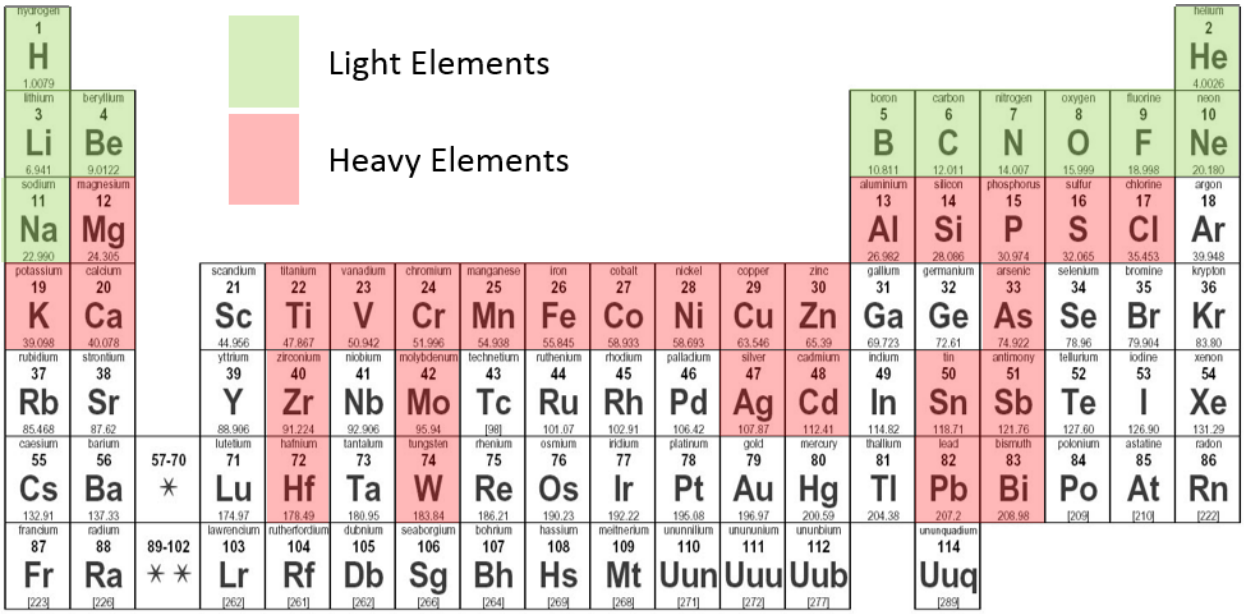

Figure 16: Periodic table showing elements measurable by the Innov-X® X-Ray Fluorescence Spectrometer (shaded).

The XRF spectrometer measures elemental abundances by subjecting the sample to X-ray photons. The high energy of the photons displaces inner orbital electrons in the respective elements. The vacancies in the lower orbitals cause outer orbital electrons to "fall" into lower orbits to satisfy the disturbed electron configuration. The substitution into lower orbitals causes a release of a secondary X-ray photon, which has an energy associated with a specific element. These relative and element specific energy emissions can then be used to determine bulk elemental composition.

2.2 MEDICAL CT SCANNING

Core scale CT scanning was performed with a medical Toshiba® Aquilion TSX-101A/R medical CT scanner as shown in Figure 17. The medical CT scanner generates images with a resolution in the millimeter range, with scans having voxel resolutions of 0.43 x 0.43 mm in the XY plane and 0.50 mm along the core axis. The scans were conducted at a voltage of 135 kV and at 200 mA. Subsequent processing and combining of stacks was performed to create three-dimensional (3D) volumetric representations of the cores and a two-dimensional (2D) cross-section through the middle of the core samples using ImageJ (Schneider et al., 2012). The variation in greyscale values observed in the images indicates changes in the CT number (CTN) obtained from the scans, which is directly proportional to changes in the attenuation and density of the scanned rock; i.e., darker regions are less dense. While the medical CT scanner was not used for detailed characterization in this study, it allowed for non-destructive bulk characterization of the core, and thus complimented the MSCL data on the resultant logs.

Figure 17: Toshiba® Aquilion™ Multislice Helical CT scanner at NETL used for core analysis.

2.3 DATA COMPILATION

Strater® by Golden Software® was used to compile the MSCL and medical CT data into a series of geophysical logs. The data used to generate these logs can be accessed from NETL's Energy Data eXchange (EDX) online system using the following link: https://edx.netl.doe.gov/dataset/roberson-smackover.

3. RESULTS

This section presents processed 2D slices of the medical CT scans through the cores, followed by the XRF and magnetic susceptibility measurements of the core from the MSCL.

3.1 MEDICAL CT SCANS

The core from the Roberson 18-19 well was scanned with a Toshiba Aquilion TSX-101A/R medical CT scanner at a sub-millimeter core-scale resolution (430 µm by 430 µm by 500 µm).

As was discussed previously, the variation in greyscale values observed in the medical CT images indicates changes in the CTN obtained, which is directly proportional to changes in the attenuation and density of the scanned rock (darker regions are less dense). Core was scanned in 3 ft or smaller sections obtained from each core box. In the following images, the overall depth for each scanned subsection of core is listed and many interesting features can readily be seen, including pyrite nodules, defined fracture planes, and fine scale layering.

3.1.1 XZ Planes

A 2D image through the center of each 3D volume was generated and the images can be found in Figures 19 through 43. These are referred to as "XZ" planes with the coordinates that are shown in Figure 18. The red scale bar shown in these images is 2 cm; the retrieved core has a diameter of 4 in. (10.16 cm) for reference. The labels below each 2D XZ plane in Figures through 43 are the depth at the bottom of each core; the full range of core lengths shown in each figure is listed in the figure captions. The greyscale values were shifted in these images to best represent the structure of the core in each image. A red 2-cm scale bar has been overlaid on each image.

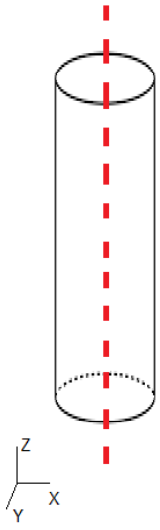

Figure 18: Schematic of the XZ isolated plane through the vertical center of the medical CT scans.

3.2 ROBERSON 18-19

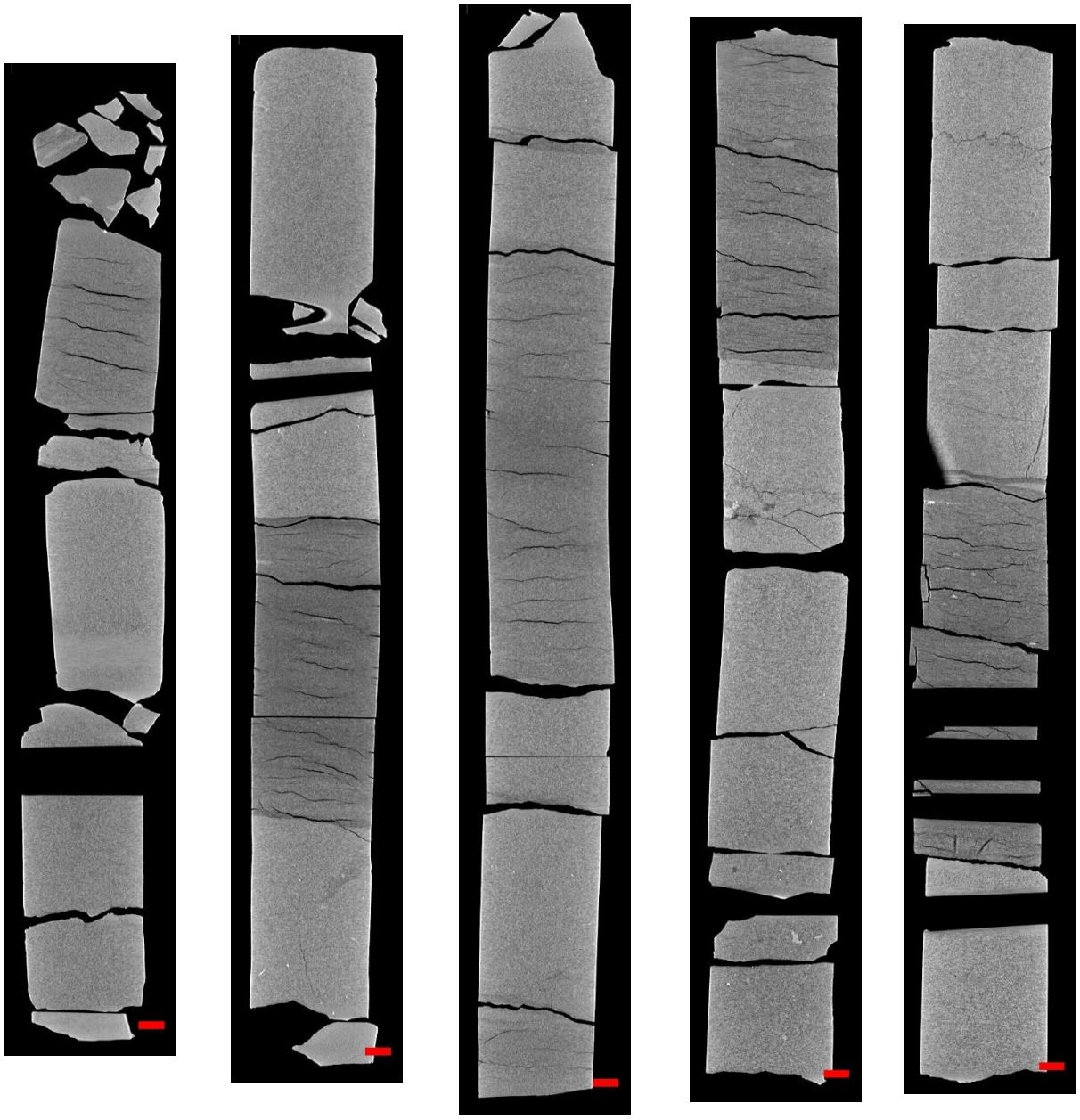

8,802–8,805 ft **8,805–8,808 ft** **8,808–8,811 ft** **8,811–8,814 ft** **8,814–8,817 ft**

Figure 19: 2D isolated planes through the vertical center of the medical CT scans of the Roberson 18-19 core from 8,802 to 8,817 ft. Red scale bar is 2 cm.

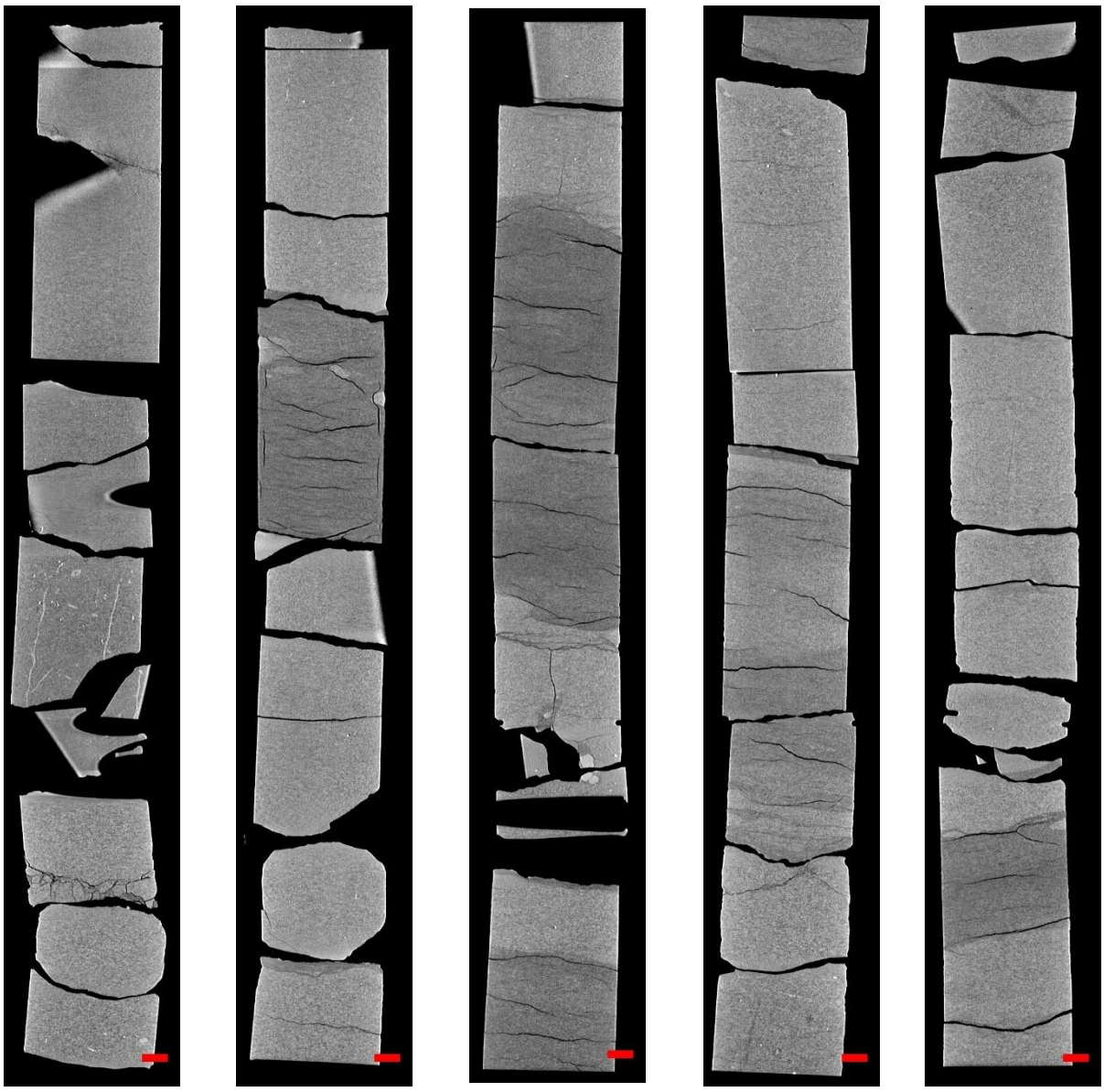

8,817–8,820 ft **8,820–8,823 ft** **8,823–8,826 ft** **8,826–8,829 ft** **8,829–8,832 ft**

Figure 20: 2D isolated planes through the vertical center of the medical CT scans of the Roberson 18-19 core from 8,817 to 8,832 ft. Red scale bar is 2 cm.

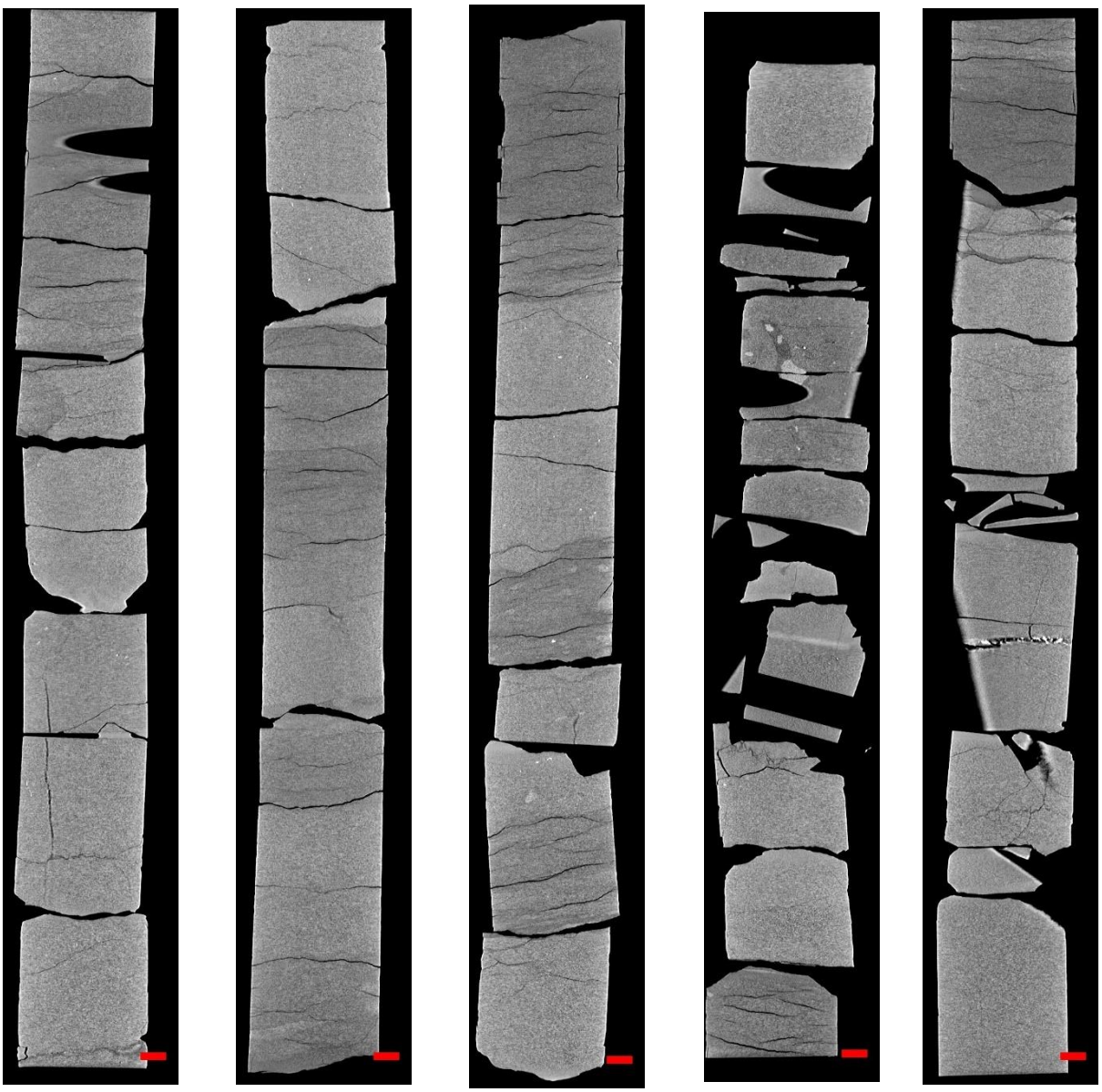

8,832–8,835 ft **8,835–8,838 ft** **8,838–8,841 ft** **8,841–8,844 ft** **8,844–8,847 ft**

Figure 21: 2D isolated planes through the vertical center of the medical CT scans of the Roberson 18-19 core from 8,832 to 8,847 ft. Red scale bar is 2 cm.

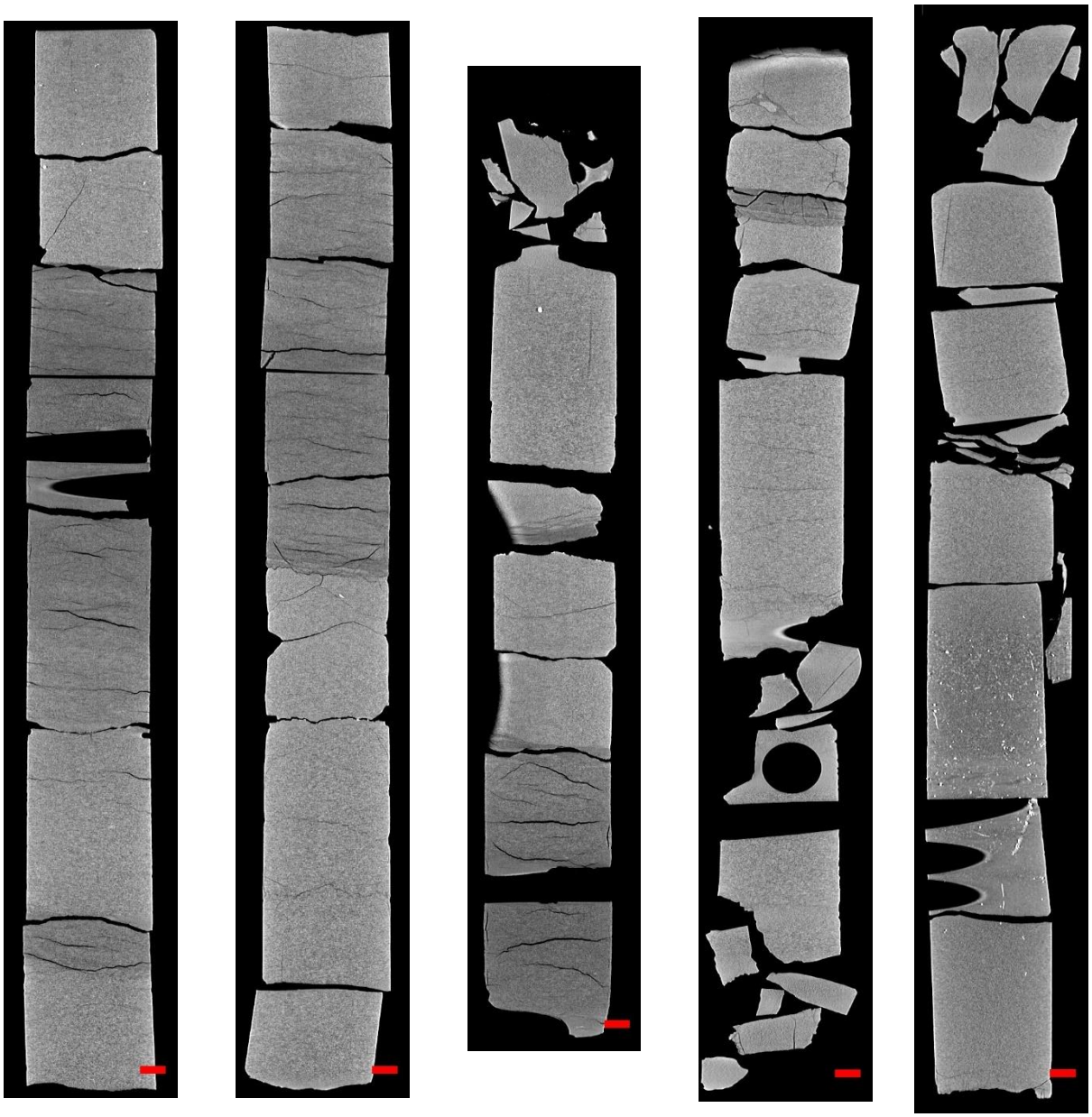

8,847–8,850 ft **8,850–8,853 ft** **8,853–8,856 ft** **8,856–8,859 ft** **8,859–8,862 ft**

Figure 22: 2D isolated planes through the vertical center of the medical CT scans of the Roberson 18-19 core from 8,847 to 8,862 ft. Red scale bar is 2 cm.

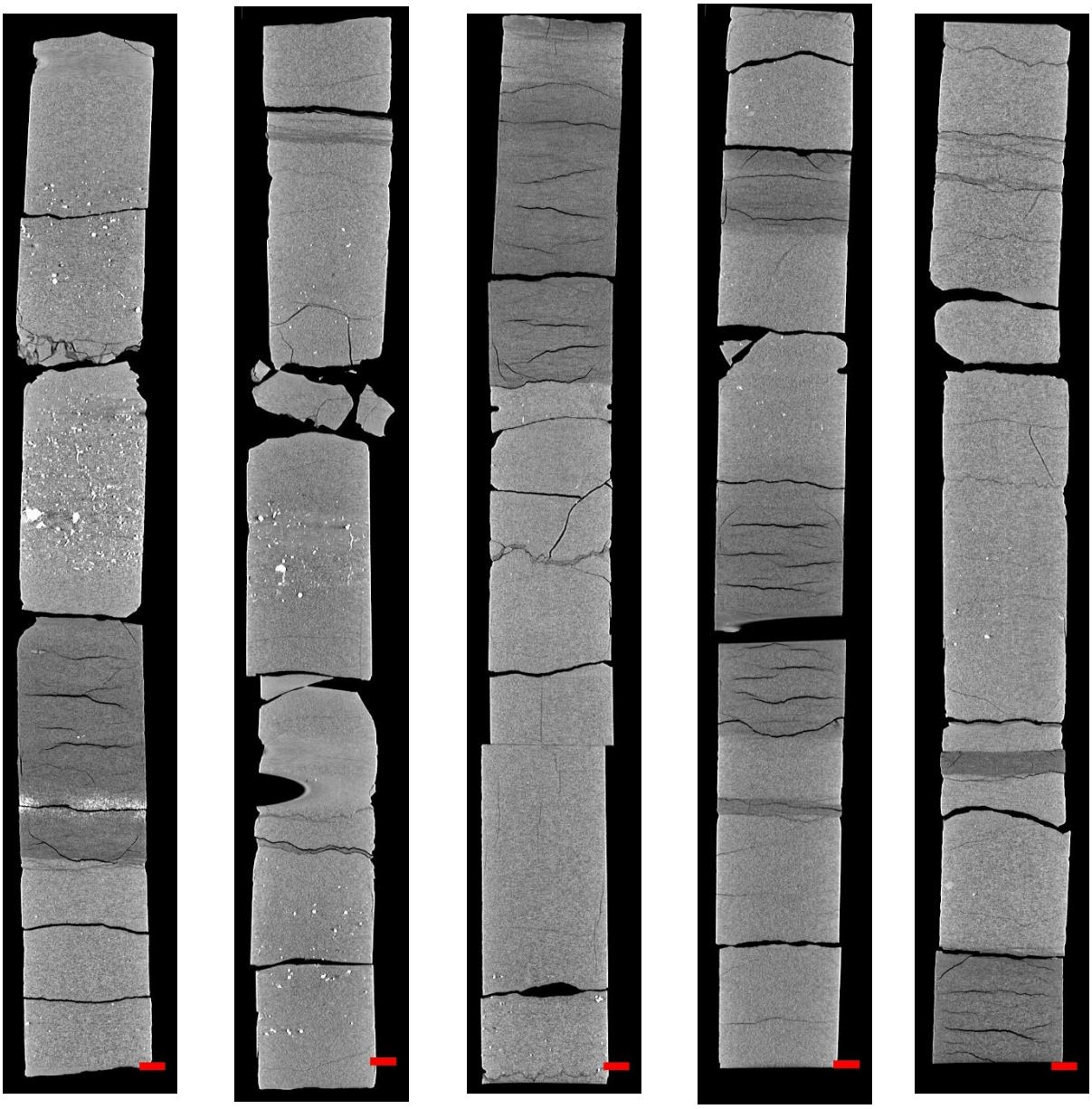

8,862–8,865 ft **8,865–8,868 ft** **8,868–8,871 ft** **8,871–8,874 ft** **8,874–8,877 ft**

Figure 23: 2D isolated planes through the vertical center of the medical CT scans of the Roberson 18-19 core from 8,862 to 8,877 ft. Red scale bar is 2 cm.

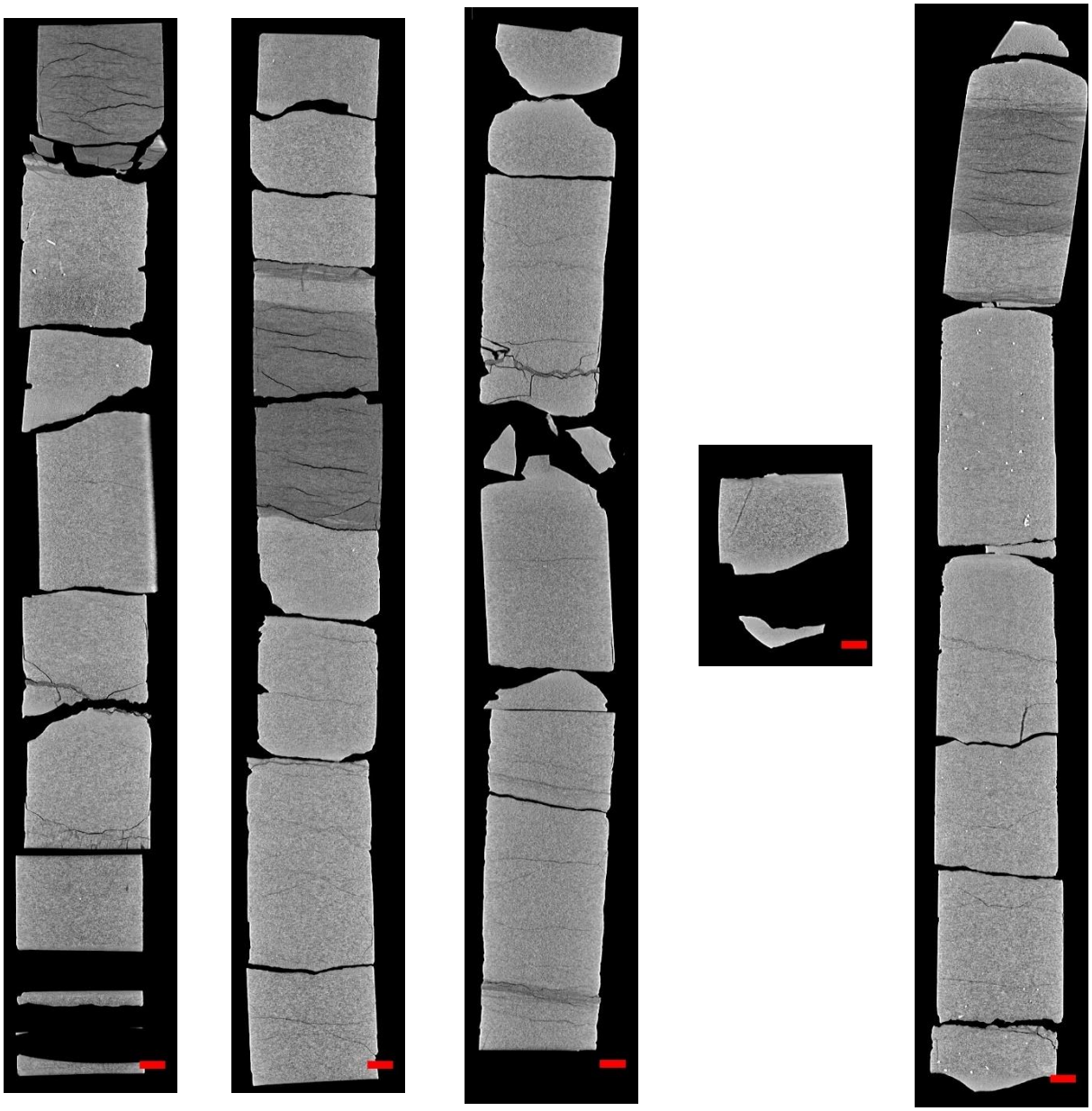

8,877–8,880 ft **8,880–8,883 ft** **8,883–8,886 ft** **8,886–8,887 ft** **8,889–8,892 ft**

Figure 24: 2D isolated planes through the vertical center of the medical CT scans of the Roberson 18-19 core from 8,877 to 8,892 ft. Red scale bar is 2 cm.

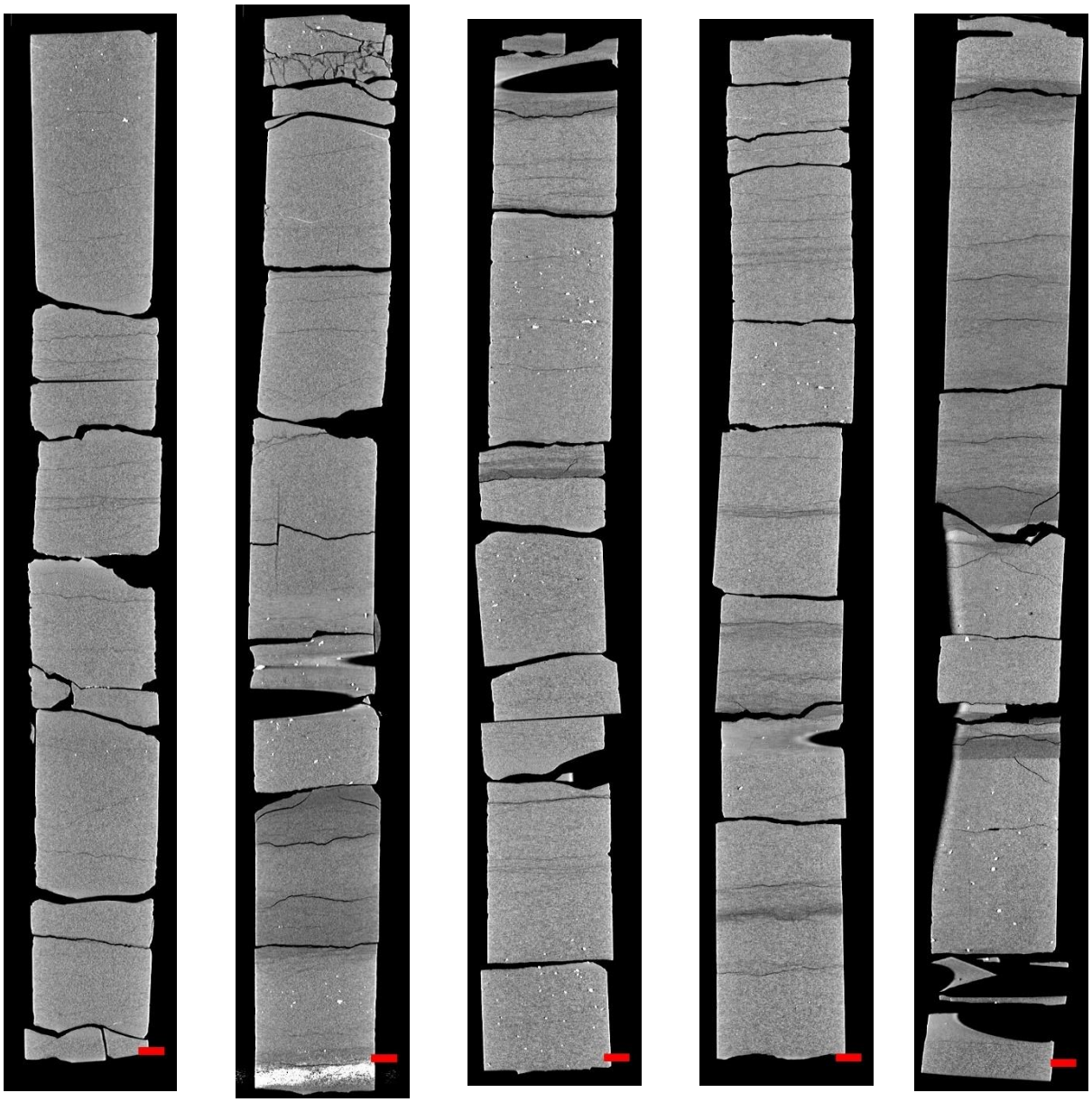

8,892–8,895 ft **8,895 –8,898 ft** **8,898–8,901 ft** **8,901–8,904 ft** **8,904–8,907 ft**

Figure 25: 2D isolated planes through the vertical center of the medical CT scans of the Roberson 18-19 core from 8,892 to 8,907 ft. Red scale bar is 2 cm.

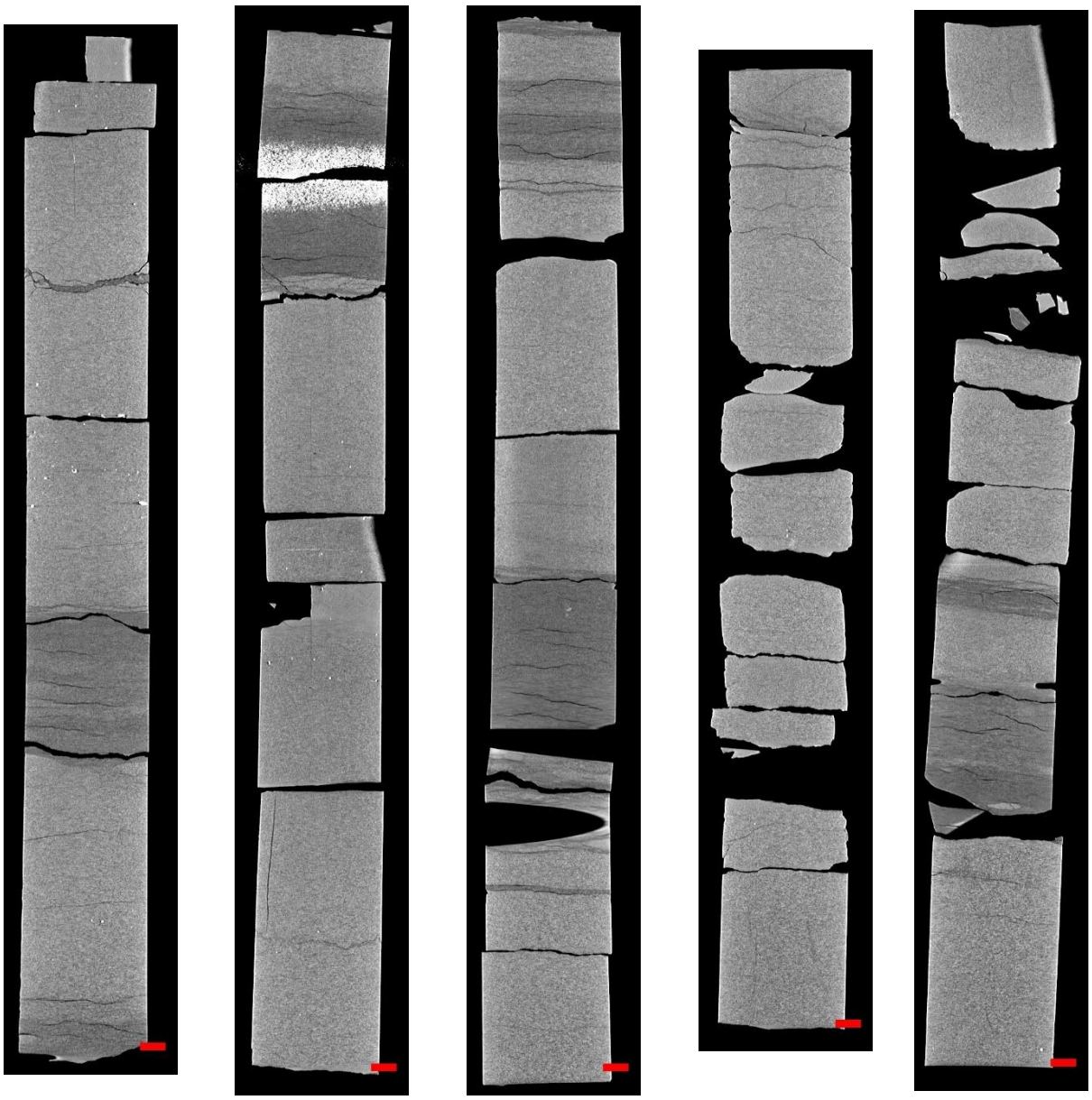

8,907–8,910 ft **8,910–8,913 ft** **8,913–8,916 ft** **8,916–8,919 ft** **8,919–8,922 ft**

Figure 26: 2D isolated planes through the vertical center of the medical CT scans of the Roberson 18-19 core from 8,907 to 8,922 ft. Red scale bar is 2 cm.

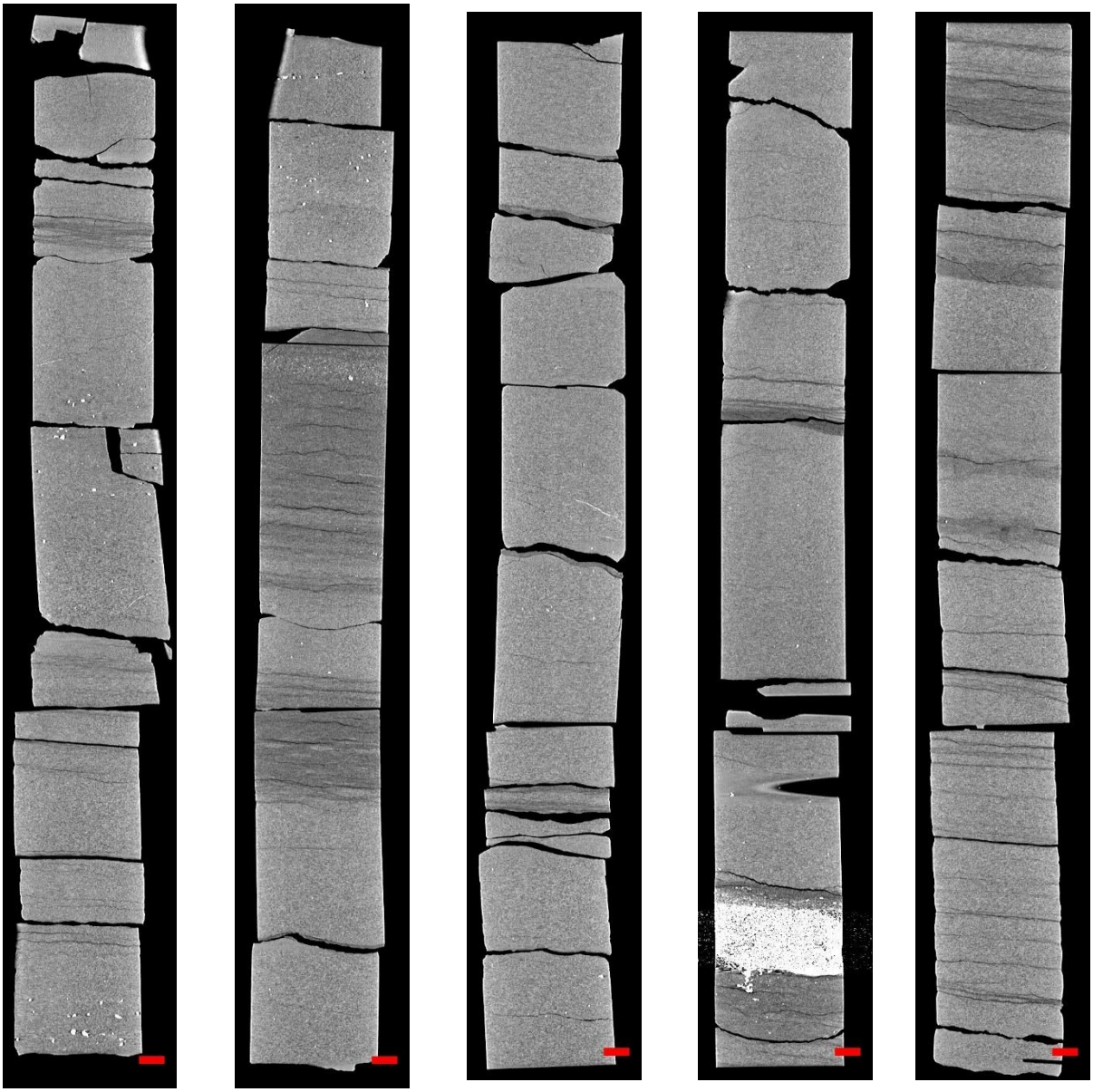

8,922–8,925 ft **8,925–8,928 ft** **8,928–8,931 ft** **8,931–8,934 ft** **8,934–8,937 ft**

Figure 27: 2D isolated planes through the vertical center of the medical CT scans of the Roberson 18-19 core from 8,922 to 8,937 ft. Red scale bar is 2 cm.

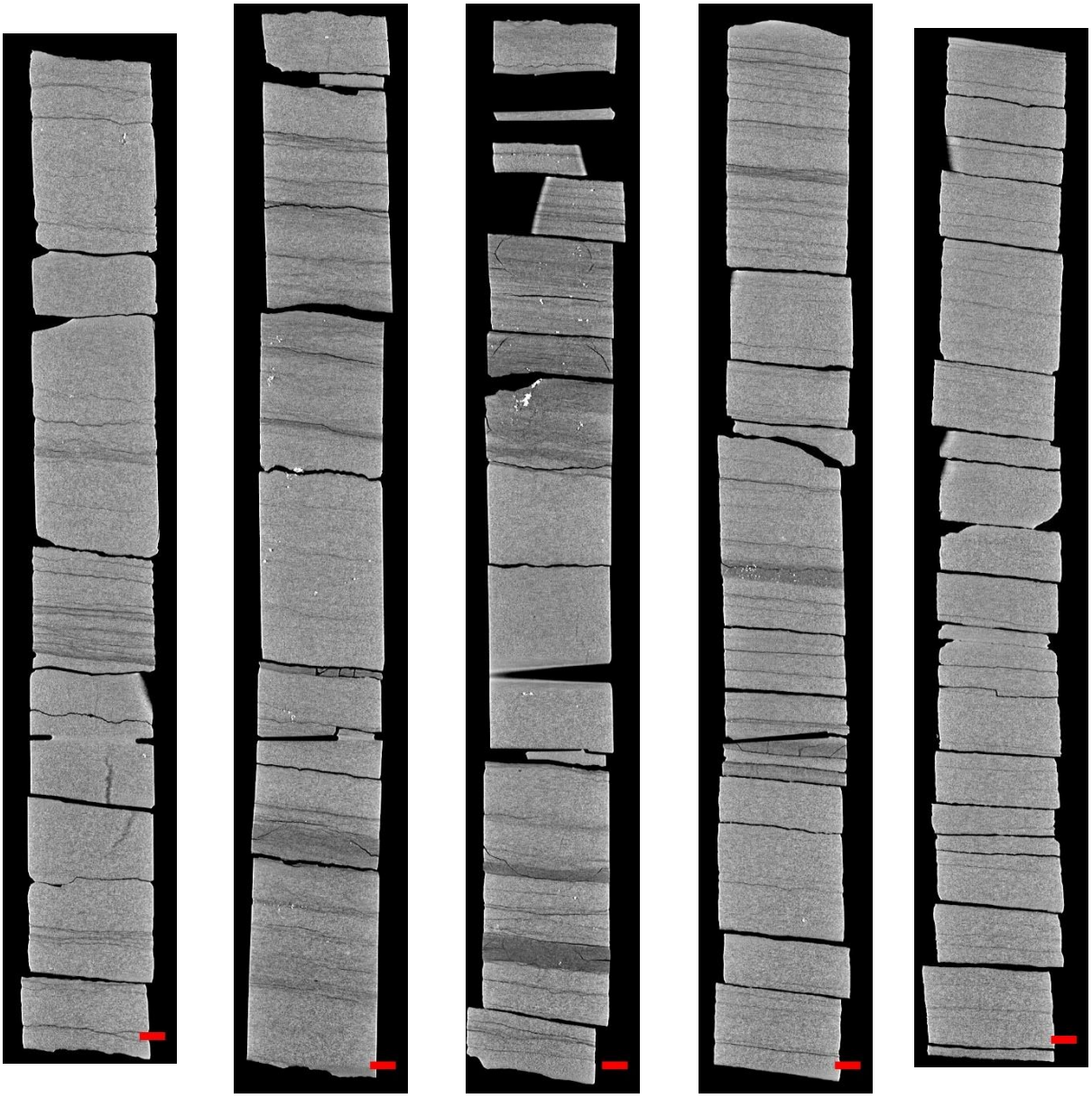

8,937–8,940 ft **8,940–8,943 ft** **8,943–8,946 ft** **8,946–8,949 ft** **8,949–8,952 ft**

Figure 28: 2D isolated planes through the vertical center of the medical CT scans of the Roberson 18-19 core from 8,937 to 8,952 ft. Red scale bar is 2 cm.

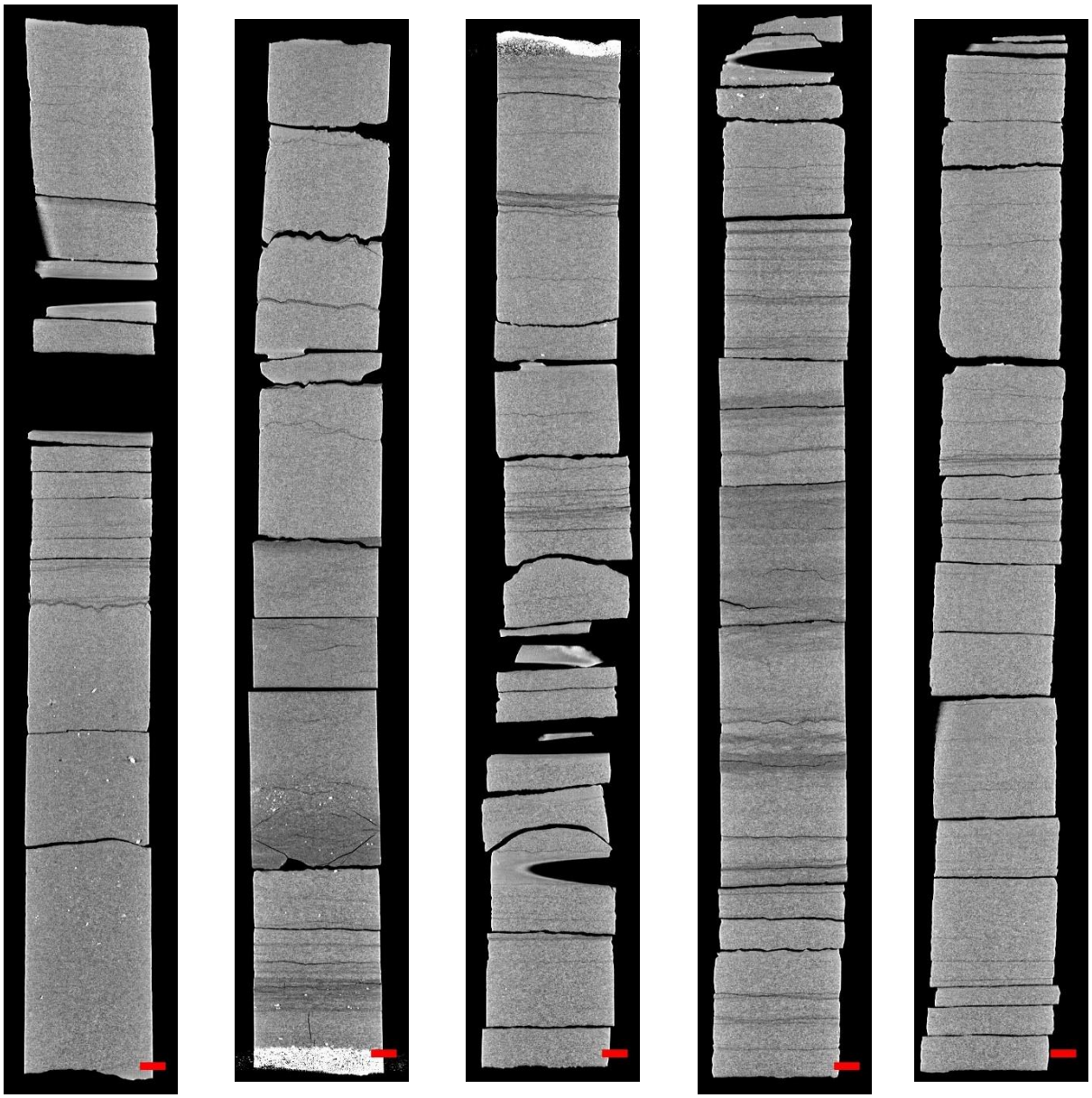

8,952–8,955 ft **8,955–8,958 ft** **8,958–8,961 ft** **8,964–8,967 ft** **8,967–8,970 ft**

Figure 29: 2D isolated planes through the vertical center of the medical CT scans of the Roberson 18-19 core from 8,952 to 8,970 ft. Red scale bar is 2 cm.

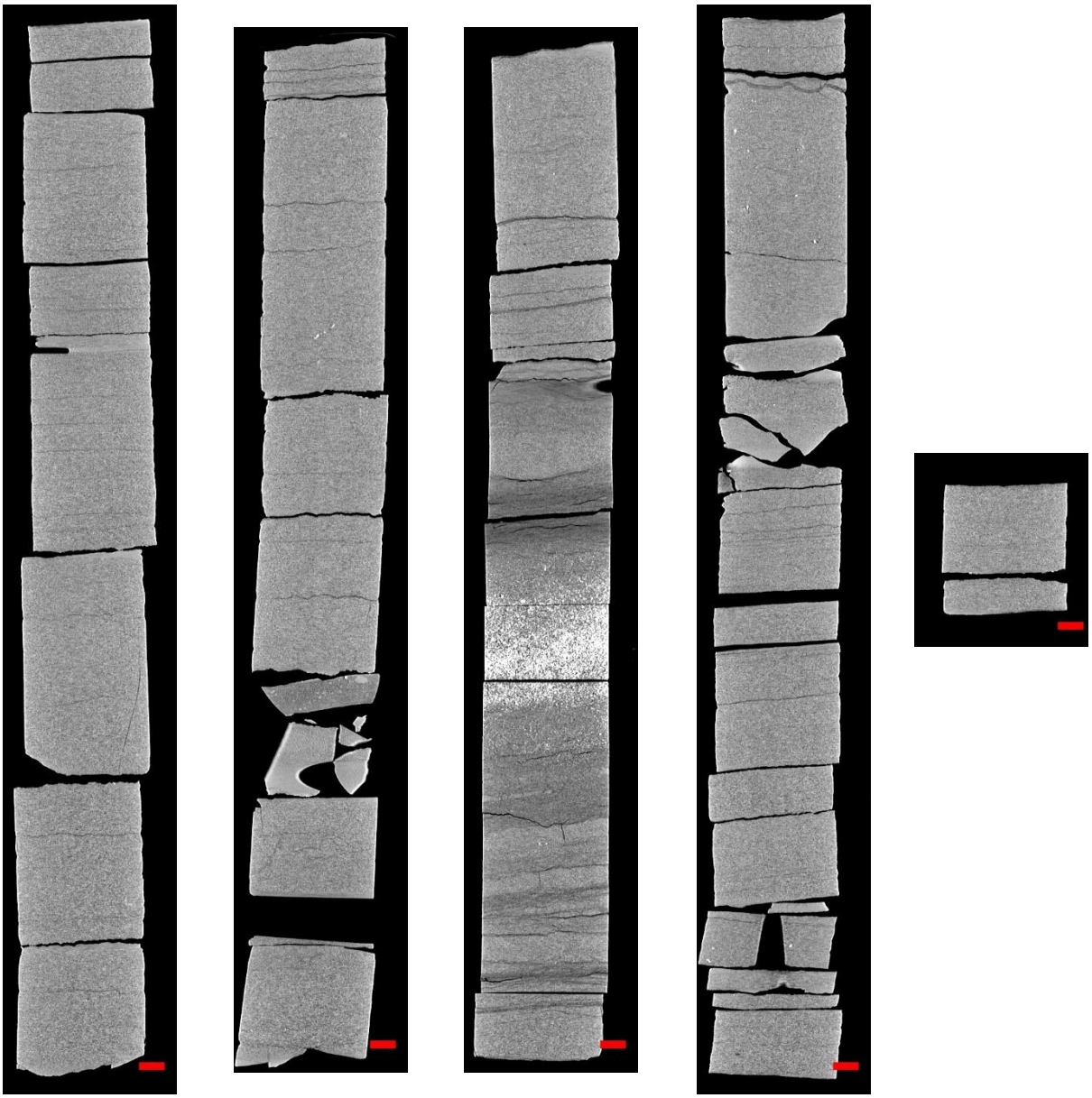

8,970–8,973 ft **8,973–8,976 ft** **8,976–8,979 ft** **8,979–8,982 ft** **8,982–8,983 ft**

Figure 30: 2D isolated planes through the vertical center of the medical CT scans of the Roberson 18-19 core from 8,970 to 8,983 ft. Red scale bar is 2 cm.

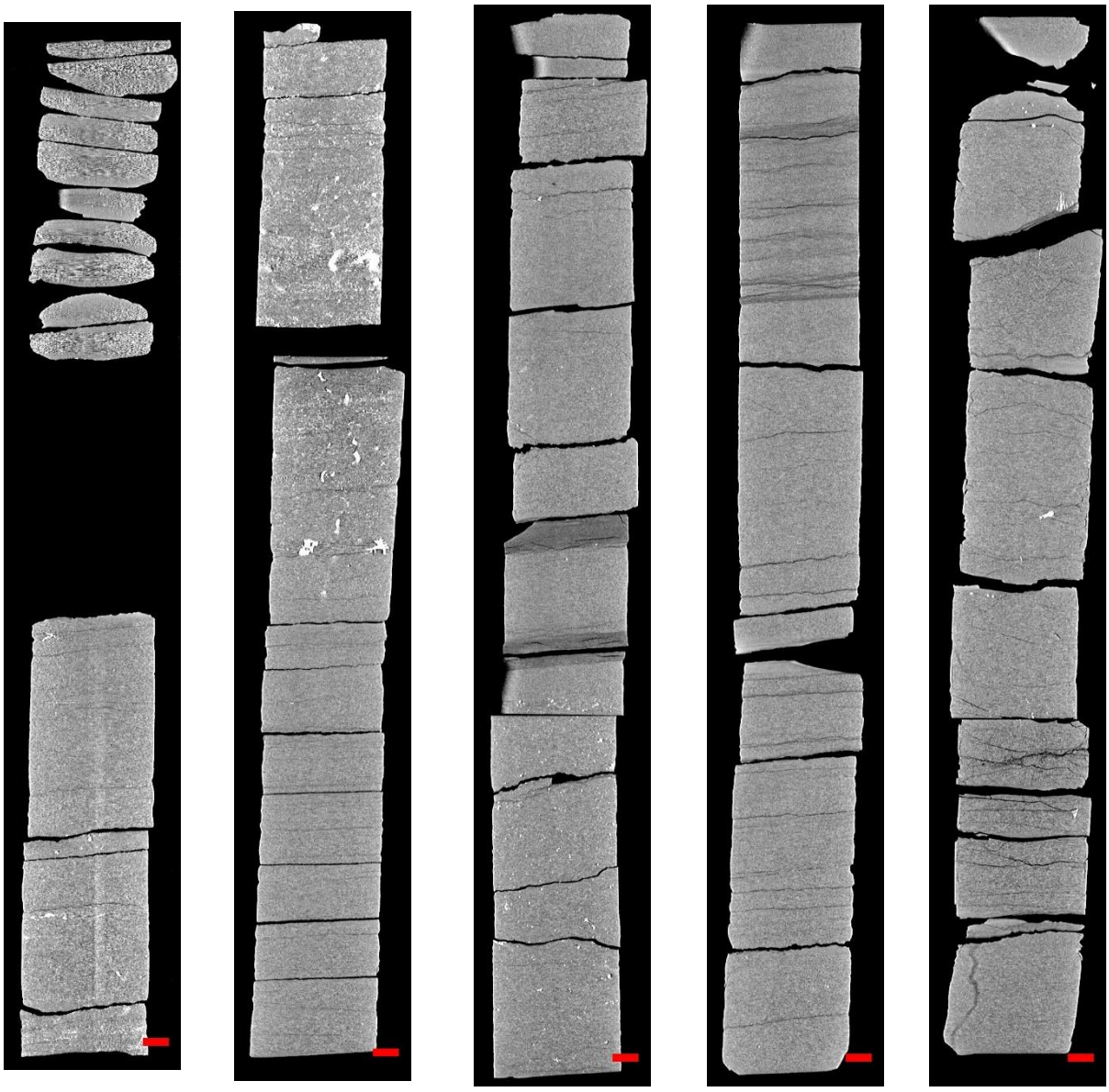

8,982–8,985 ft **8,985–8,988 ft** **8,988–8,991 ft** **8,991–8,994 ft** **8,994–8,997 ft**

Figure 31: 2D isolated planes through the vertical center of the medical CT scans of the Roberson 18-19 core from 8,982 to 8,997 ft. Red scale bar is 2 cm.

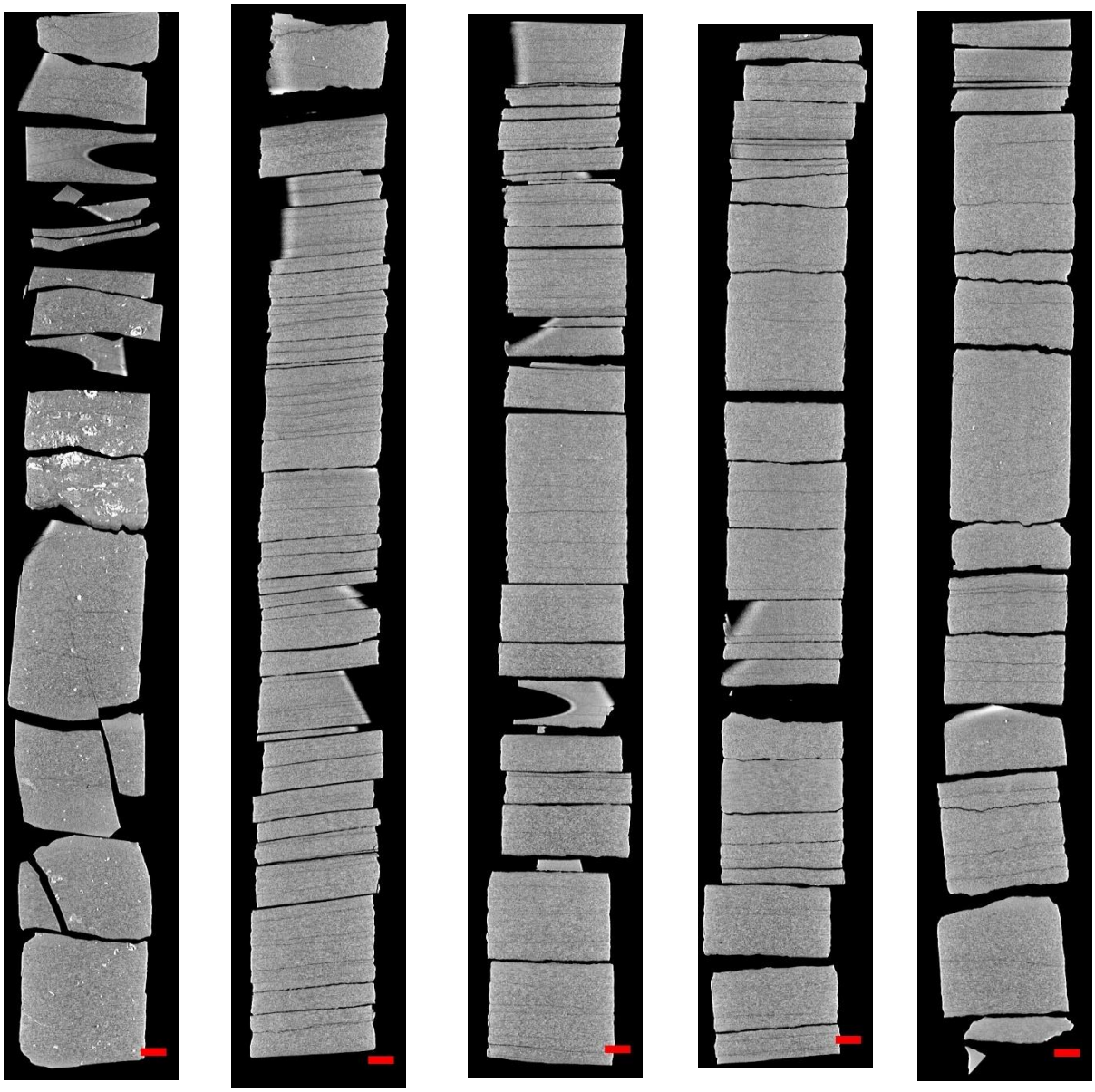

8,997–9,000 ft **9,000–9,003 ft** **9,003–9,006 ft** **9,006–9,009 ft** **9,009–9,012 ft**

Figure 32: 2D isolated planes through the vertical center of the medical CT scans of the Roberson 18-19 core from 8,997 to 9,012 ft. Red scale bar is 2 cm.

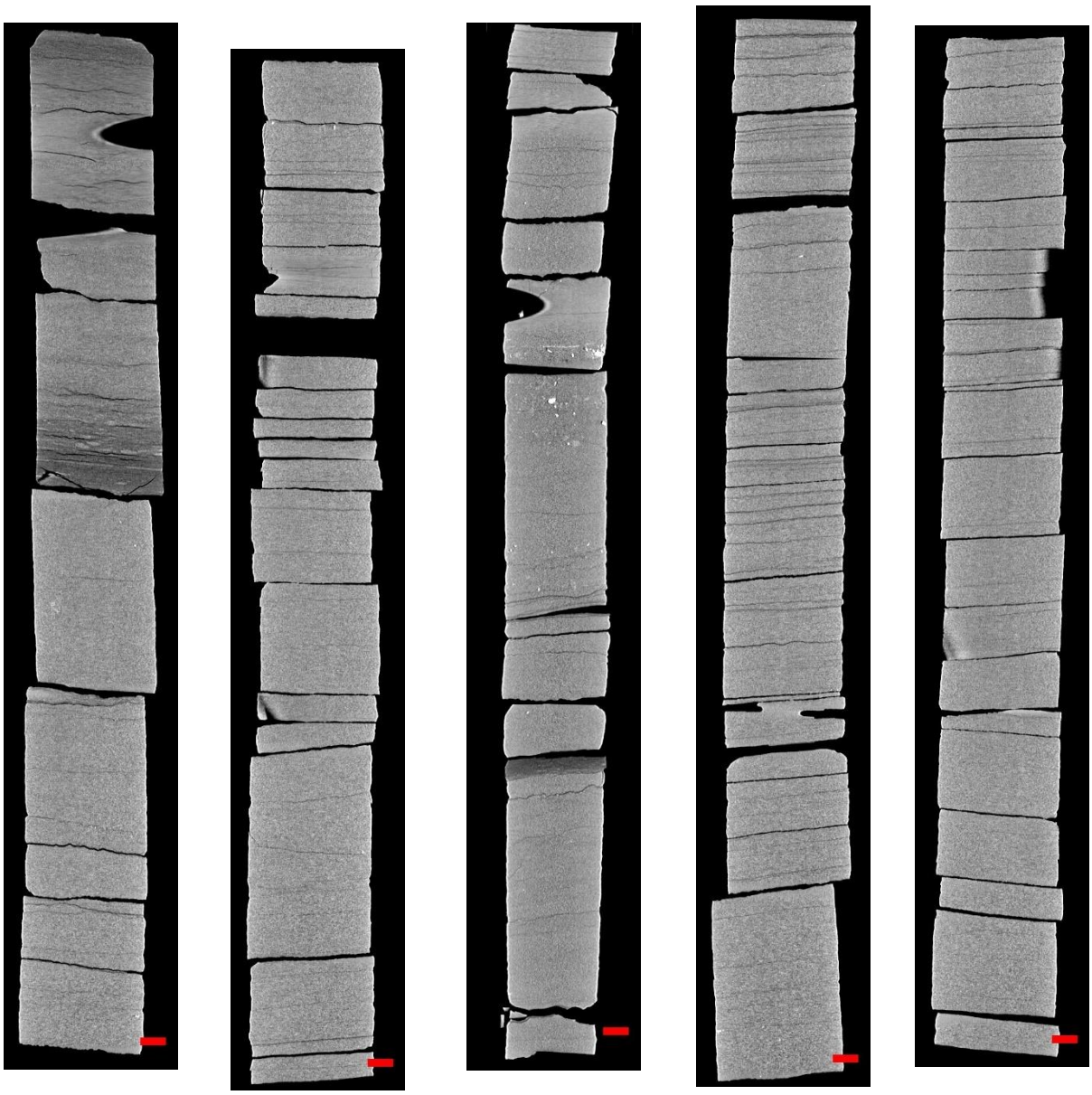

9,012–9,015 ft **9,015–9,018 ft** **9,018–9,021 ft** **9,021–9,024 ft** **9,024–9,027 ft**

Figure 33: 2D isolated planes through the vertical center of the medical CT scans of the Roberson 18-19 core from 9,012 to 9,027 ft. Red scale bar is 2 cm.

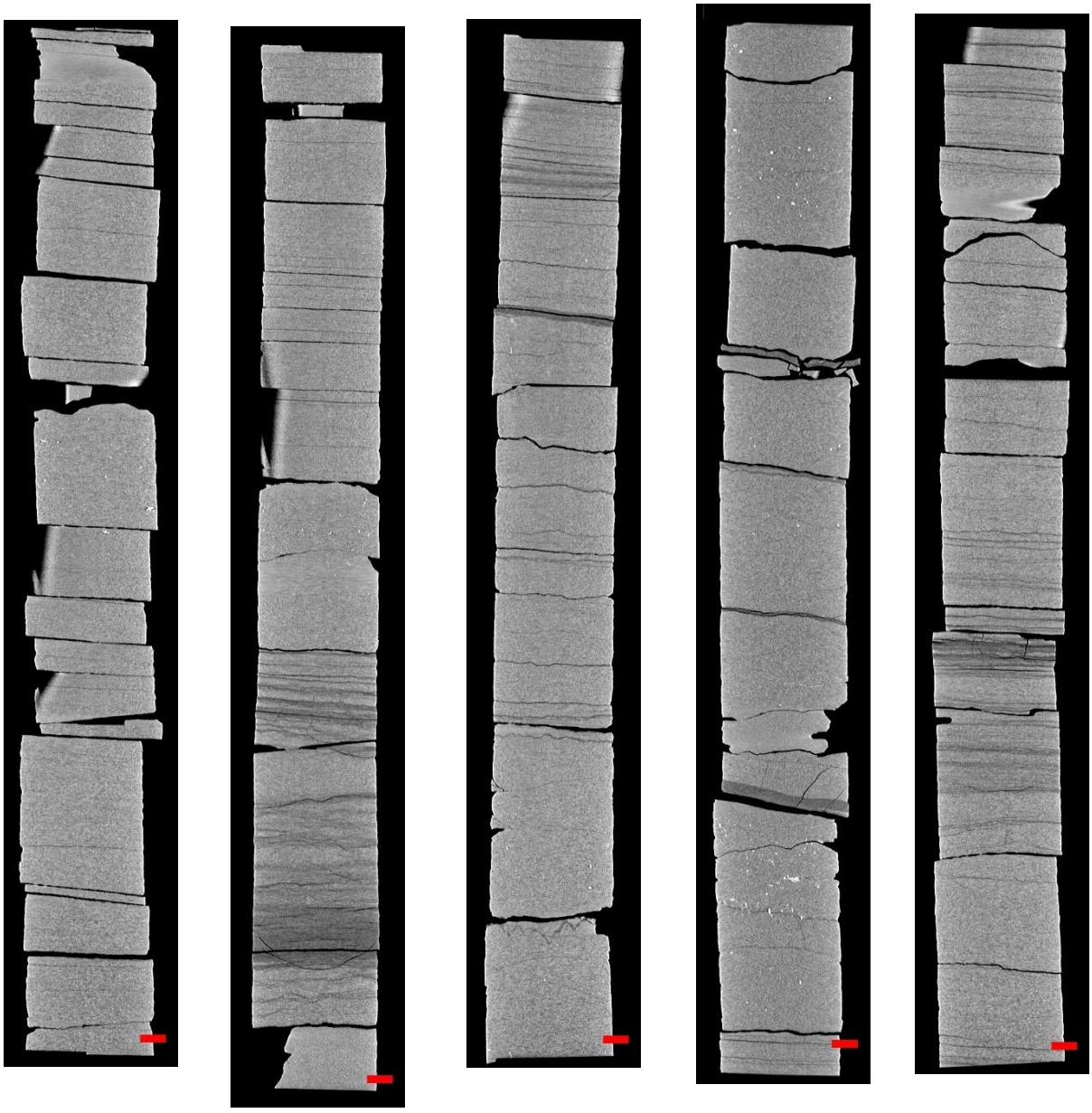

9,027–9,030 ft **9,030–9,033 ft** **9,033–9,036 ft** **9,036–9,039 ft** **9,039–9,042 ft**

Figure 34: 2D isolated planes through the vertical center of the medical CT scans of the Roberson 18-19 core from 9,027 to 9,042. Red scale bar is 2 cm.

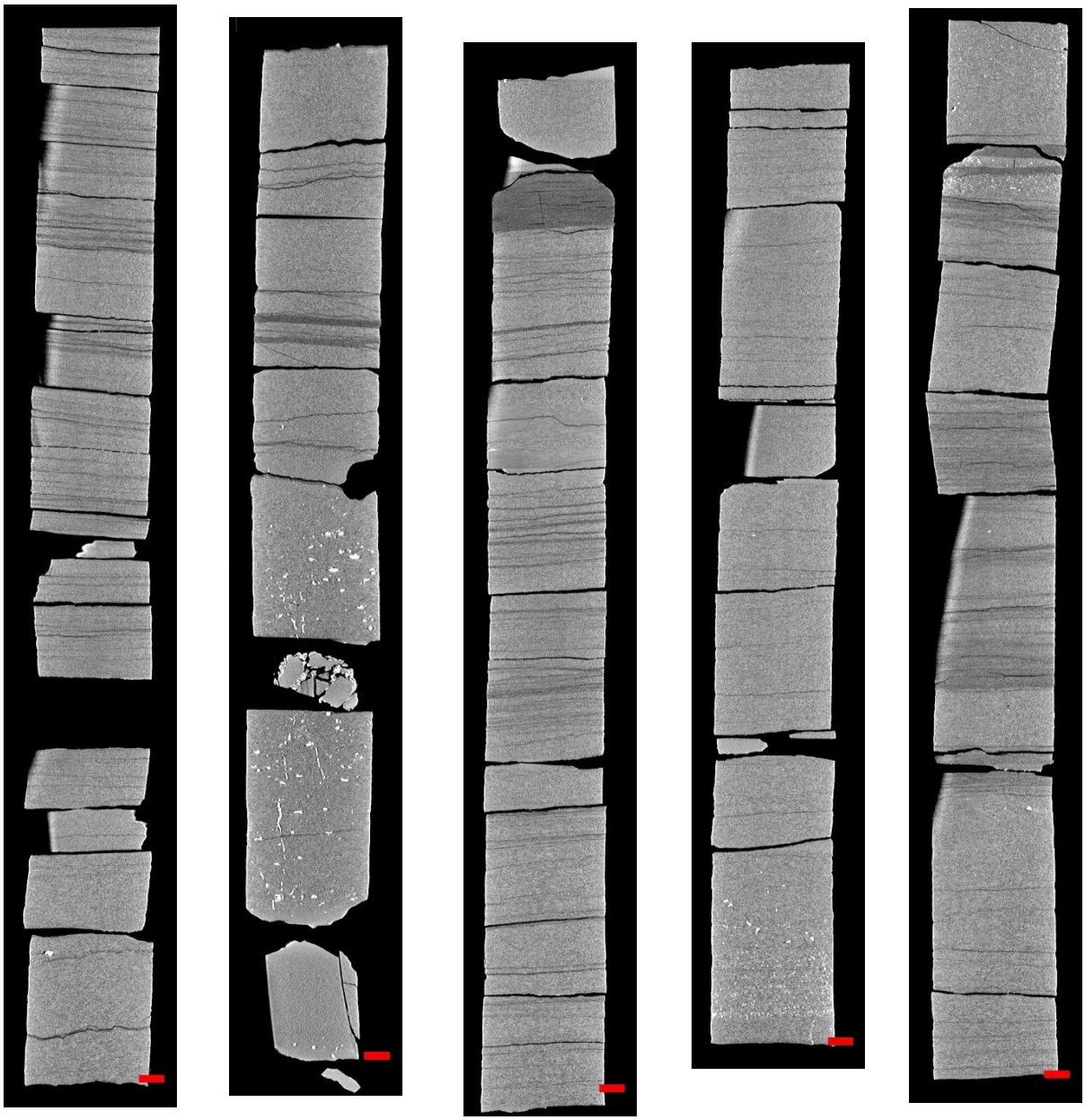

9,042–9,045 ft **9,045–9,048 ft** **9,048–9,051 ft** **9,051–9,054 ft** **9,054–9,057 ft**

Figure 35: 2D isolated planes through the vertical center of the medical CT scans of the Roberson 18-19 core from 9,042 to 9,057 ft. Red scale bar is 2 cm.

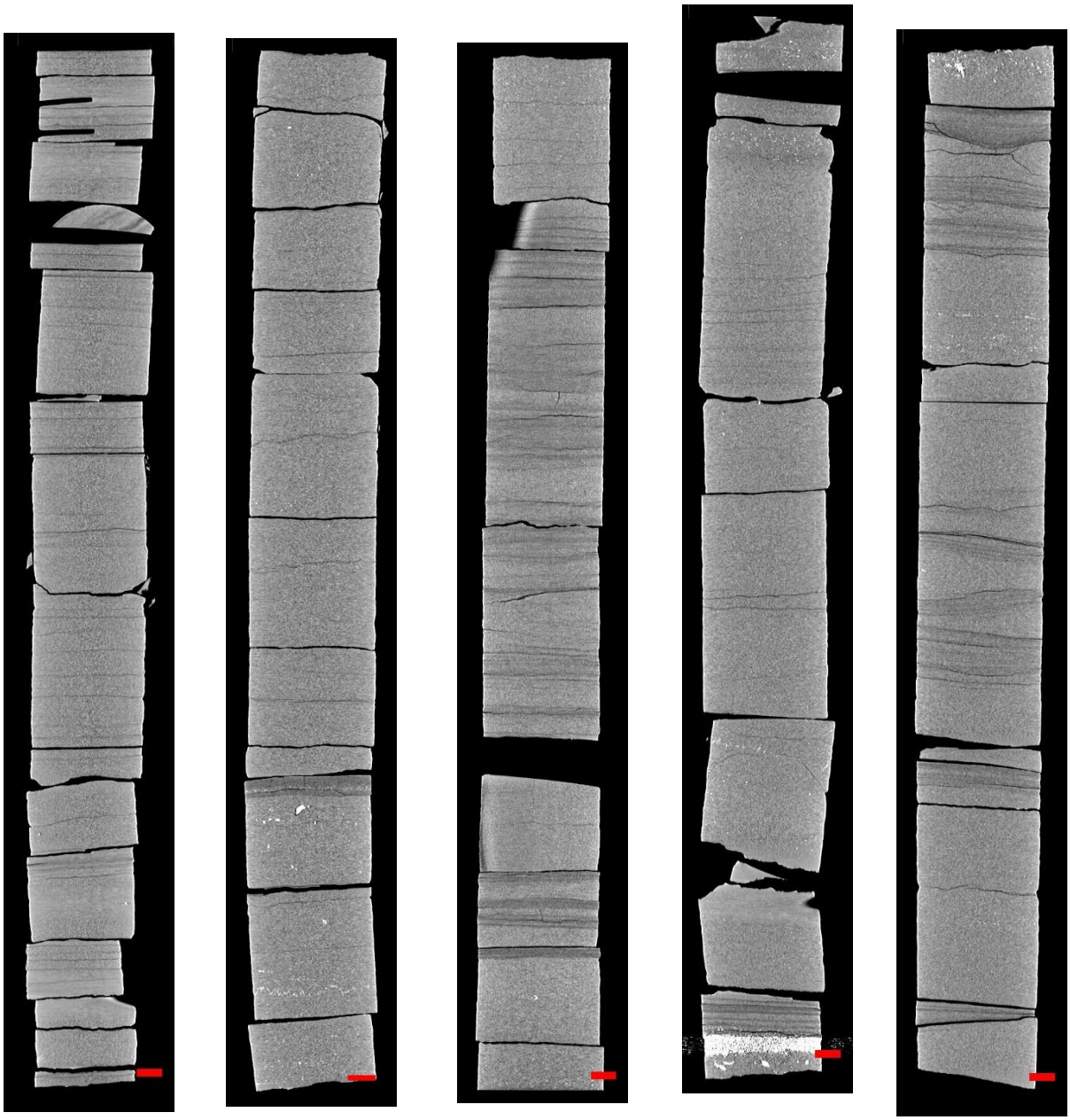

9,057–9,060 ft **9,060–9,063 ft** **9,063–9,066 ft** **9,066–9,069 ft** **9,069–9,072 ft**

Figure 36: 2D isolated planes through the vertical center of the medical CT scans of the Roberson 18-19 core from 9,057 to 9,072 ft. Red scale bar is 2 cm.

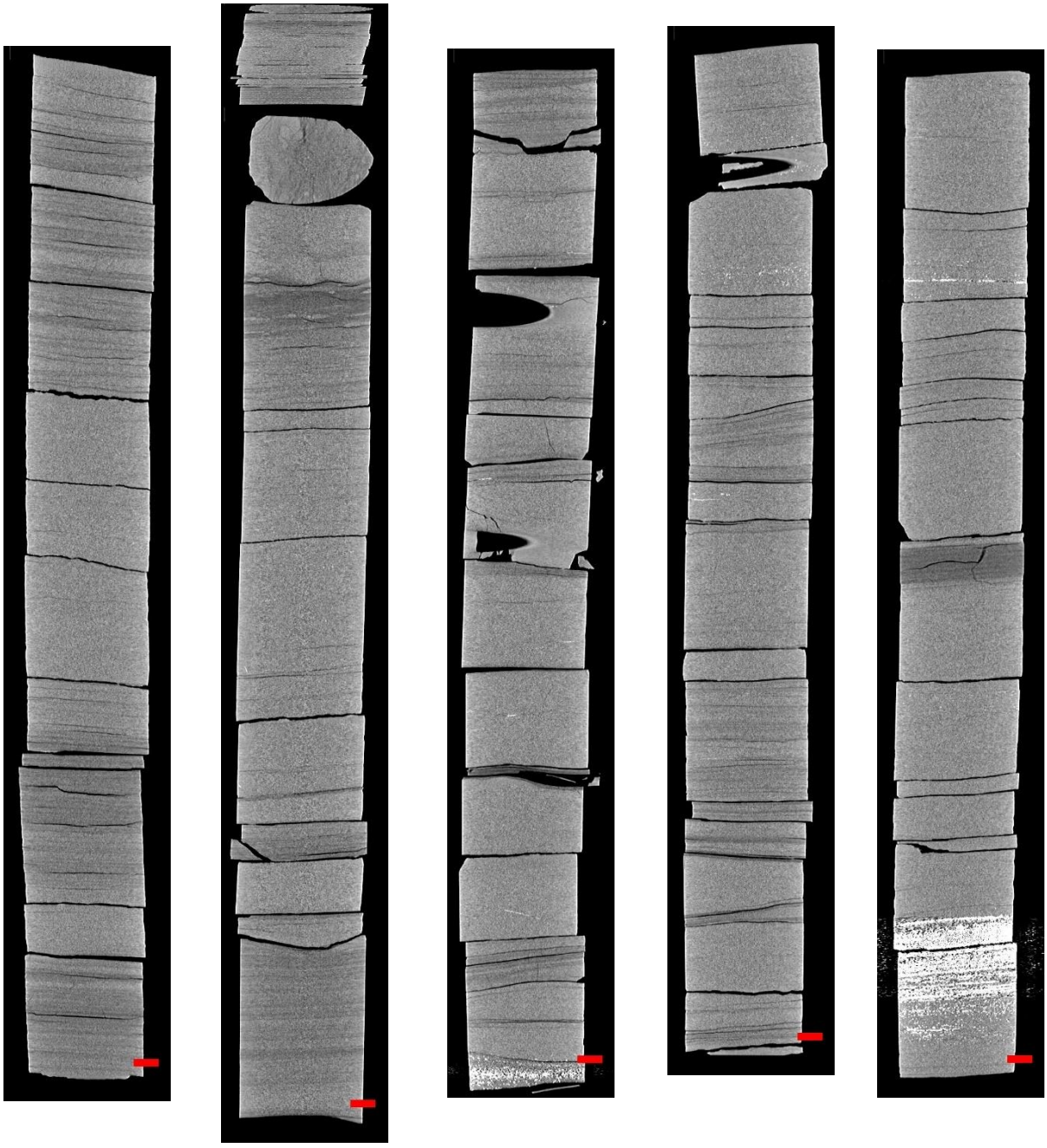

9,072–9,076 ft **9,076–9,078 ft** **9,078–9,081 ft** **9,081–9,084 ft** **9,084–9,087 ft**

Figure 37: 2D isolated planes through the vertical center of the medical CT scans of the Roberson 18-19 core from 9,072 to 9,087 ft. Red scale bar is 2 cm.

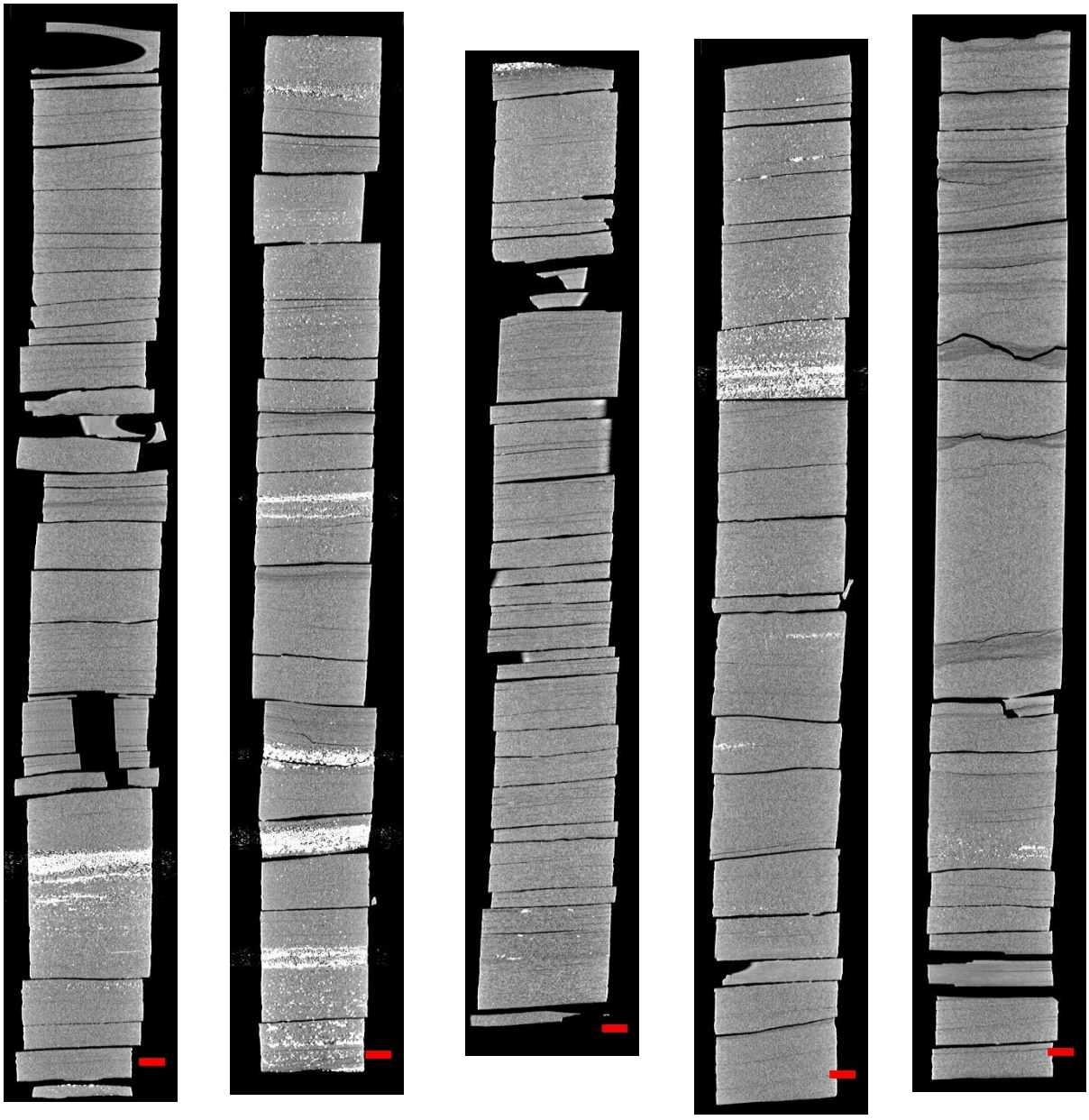

9,087–9,090 ft **9,090–9,093 ft** **9,093–9,096 ft** **9,096–9,099 ft** **9,099–9,102 ft**

Figure 38: 2D isolated planes through the vertical center of the medical CT scans of the Roberson 18-19 core from 9,087 to 9,102 ft. Red scale bar is 2 cm.

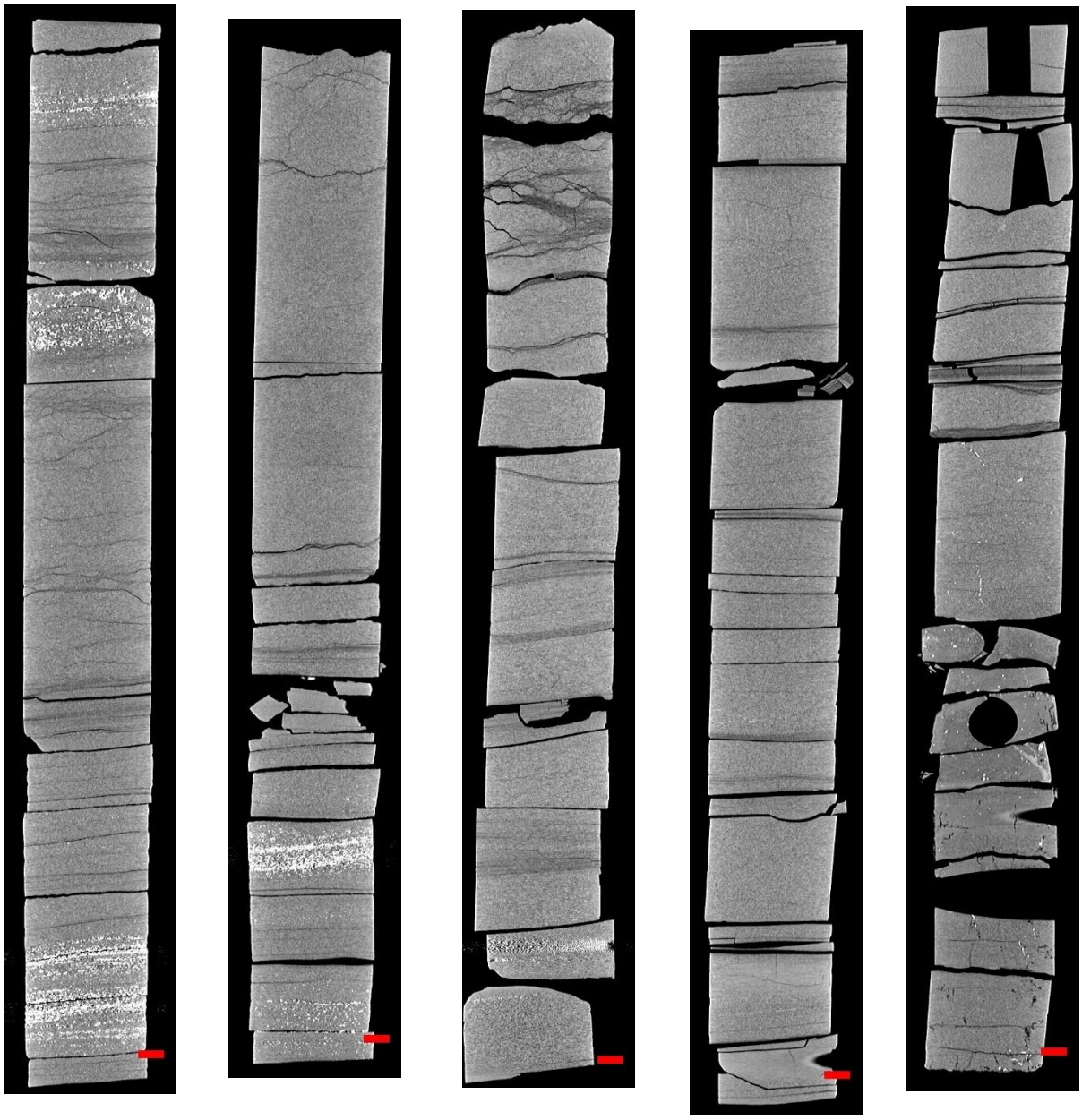

9,102–9,105 ft **9,105–9,108 ft** **9,108–9,111 ft** **9,111–9,114 ft** **9,114–9,117 ft**

Figure 39: 2D isolated planes through the vertical center of the medical CT scans of the Roberson 18-19 core from 9,102 to 9,117 ft. Red scale bar is 2 cm.

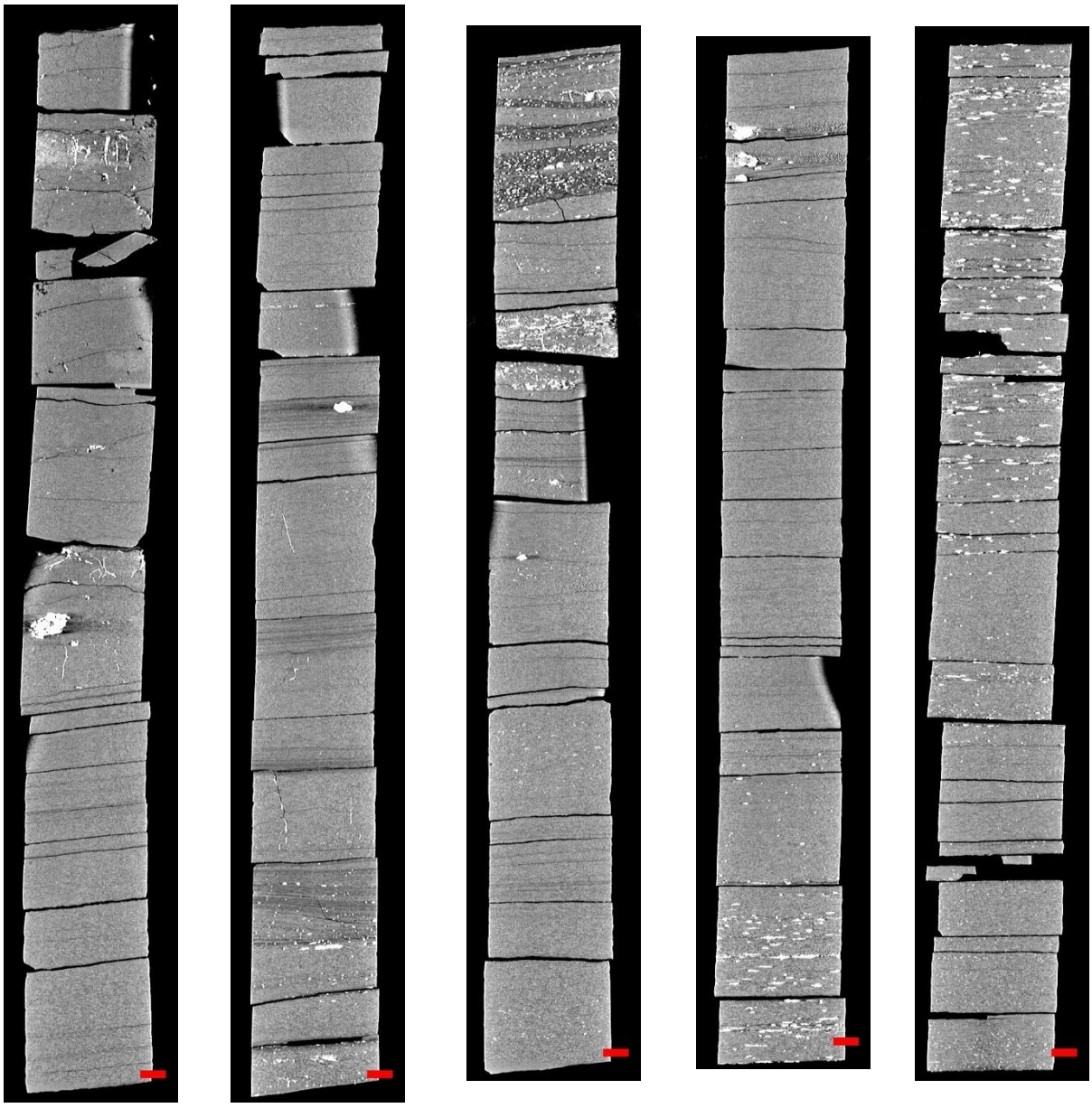

9,117–9,120 ft **9,120–9,123 ft** **9,123–9,126 ft** **9,126–9,129 ft** **9,129–9,132 ft**

Figure 40: 2D isolated planes through the vertical center of the medical CT scans of the Roberson 18-19 core from 9,117 to 9,132 ft. Red scale bar is 2 cm.

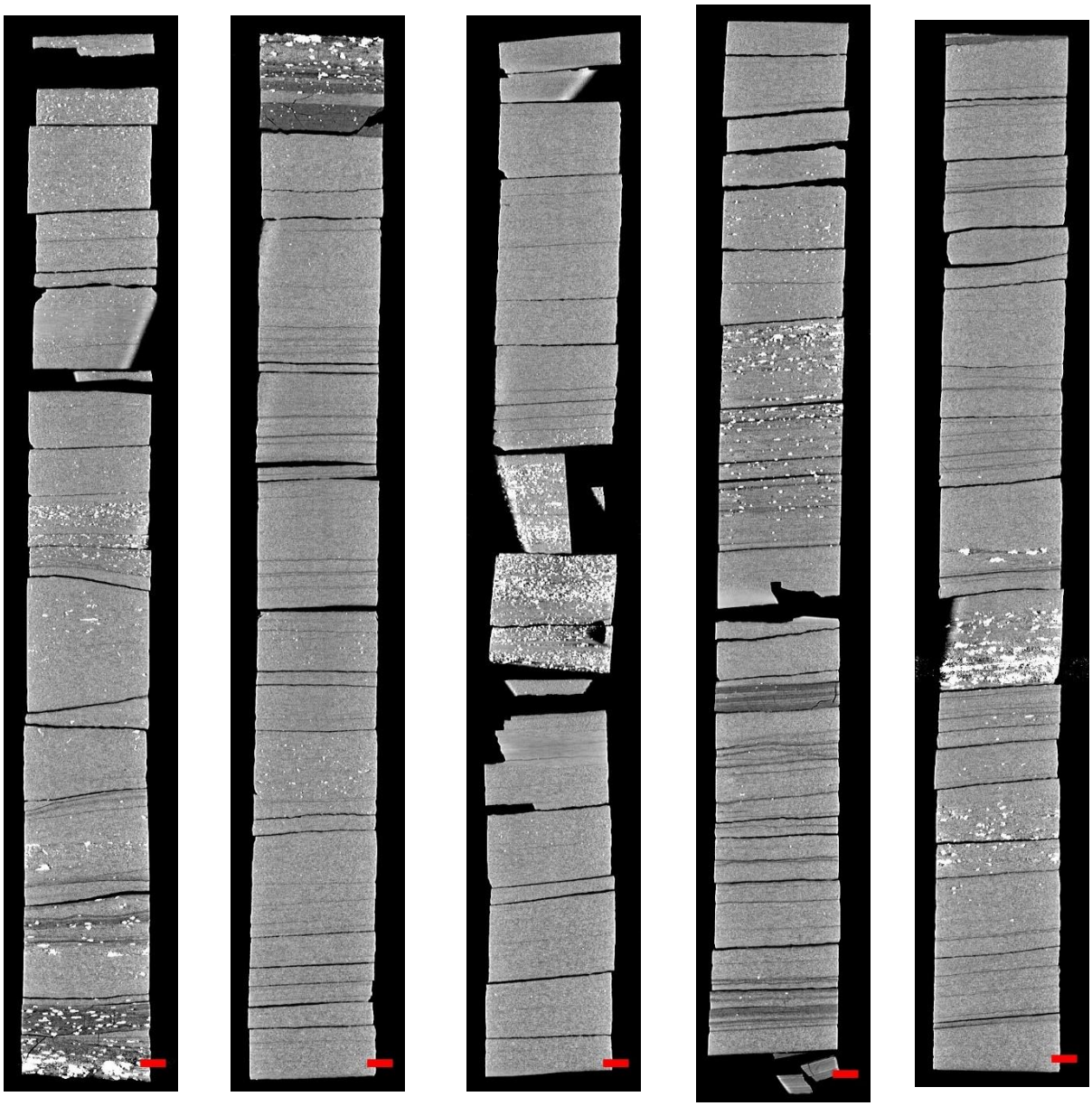

9,132–9,135 ft **9,135–9,138 ft** **9,138–9,141 ft** **9,141–9,144 ft** **9,144–9,147 ft**

Figure 41: 2D isolated planes through the vertical center of the medical CT scans of the Roberson 18-19 core from 9,132 to 9,147 ft. Red scale bar is 2 cm.

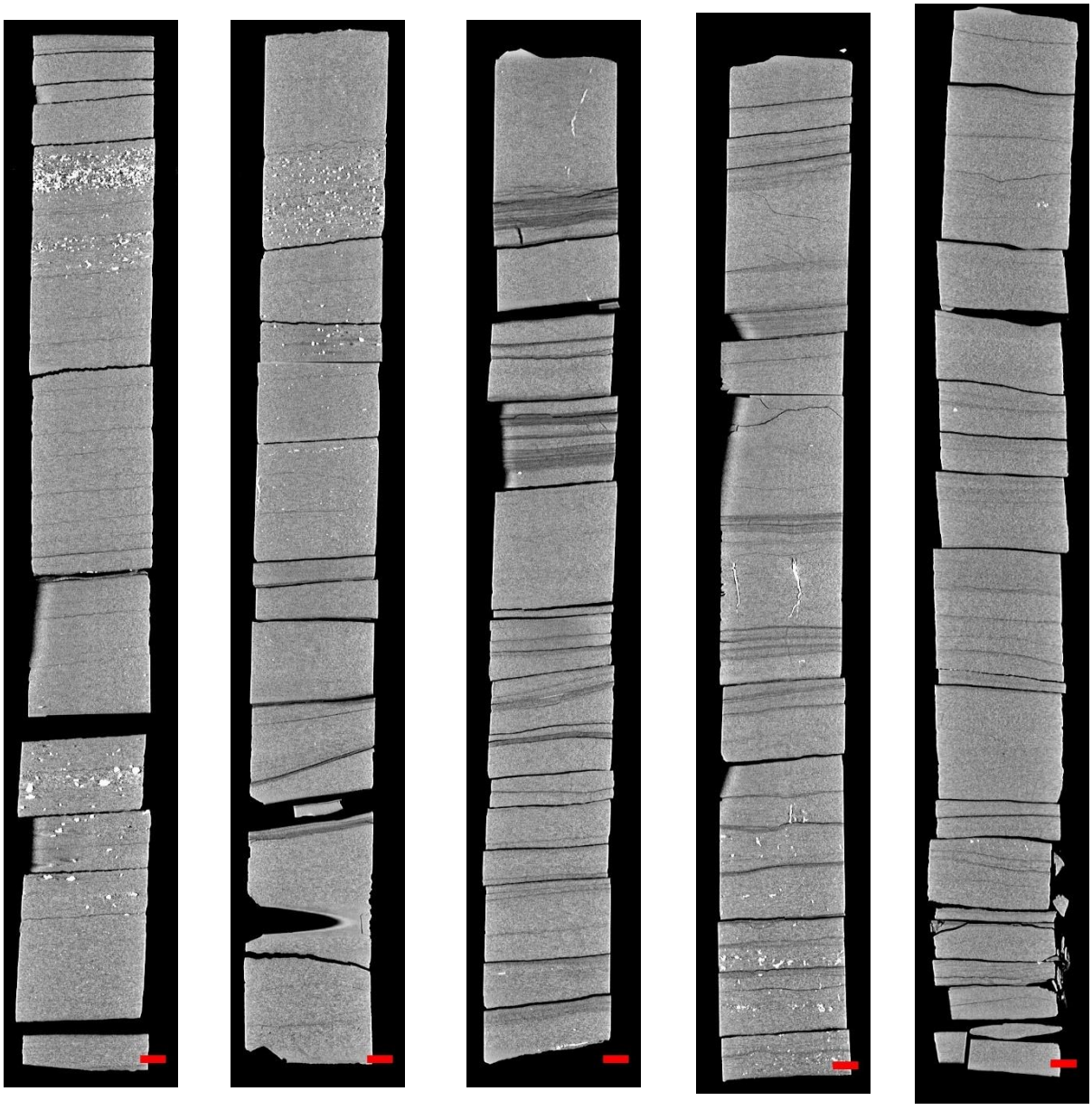

9,147–9,150 ft **9,150–9,153 ft** **9,153–9,156 ft** **9,156–9,159 ft** **9,159–9,162 ft**

Figure 42: 2D isolated planes through the vertical center of the medical CT scans of the Roberson 18-19 core from 9,147 to 9,162 ft. Red scale bar is 2 cm.

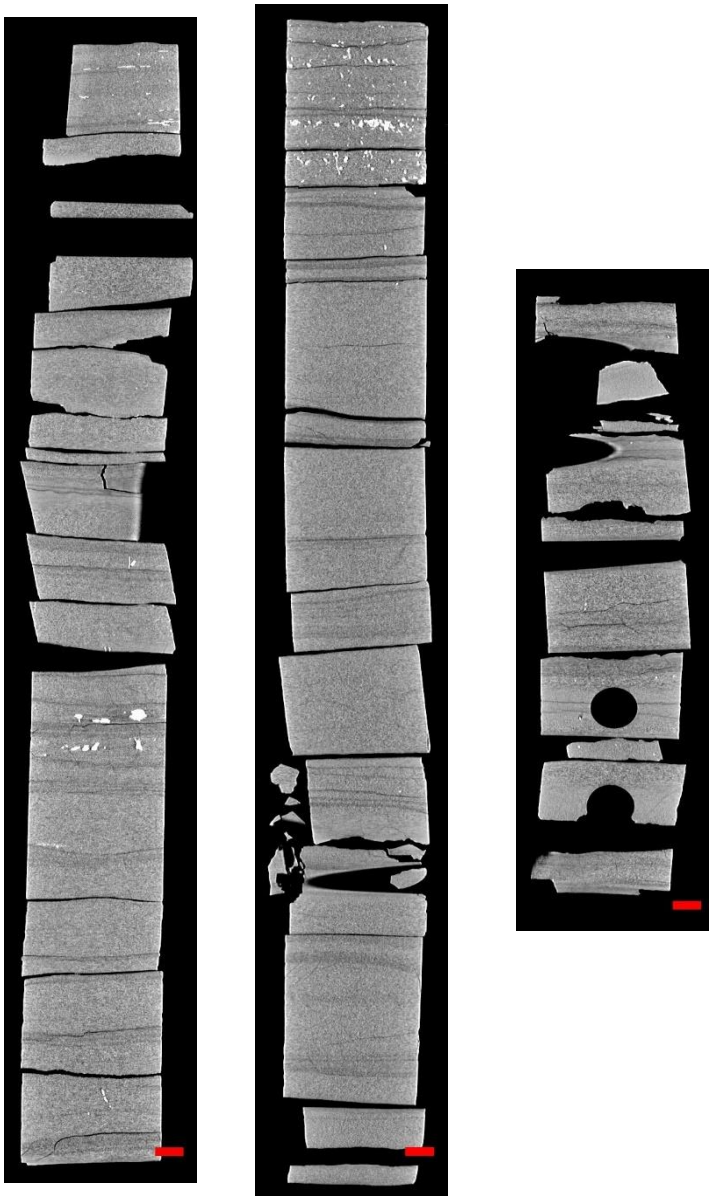

9,162–9,165 ft **9,165–9,168 ft** **9,168–9,170 ft**

Figure 43: 2D isolated planes through the vertical center of the medical CT scans of the Roberson 18-19 core from 9,162 to 9,170 ft. Red scale bar is 2 cm.

3.3 ADDITIONAL CT DATA

Additional CT data can be accessed from NETL's EDX online system using the following link: https://edx.netl.doe.gov/dataset/roberson-smackover. The original CT data is available as 16-bit tif stacks suitable for reading with ImageJ (Schneider et al., 2012) or other image analysis software.

3.3.1 Medical CT Image Videos

In addition to the CT data, videos showing the variation along the length of the cross-section images shown in the previous section are available for download and viewing on EDX. A single image from these videos is shown in Figure 44, where the distribution of high-density minerals in a cross section of the core from a depth of 9,129 to 9,132 ft is shown. Here, the red line through the XZ-plane on the image of the core shows the location of the XY-plane displayed above. The videos on EDX show this XY variation along the entire length of the core.

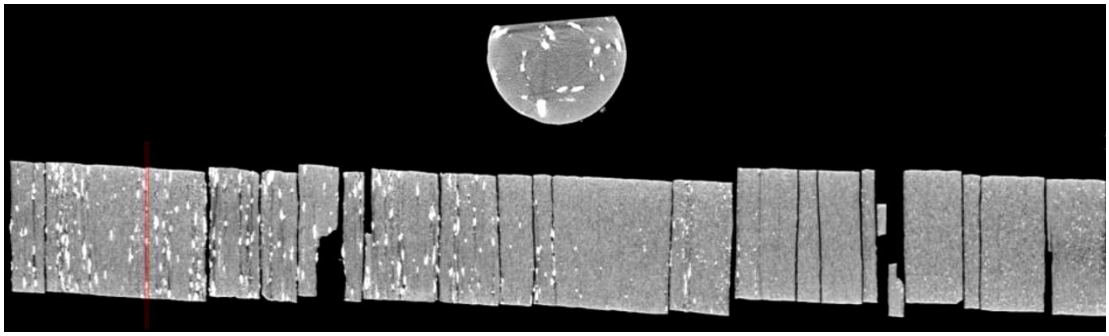

Figure 44: Single image from a video file available on EDX showing variation in the Roberson 18-19 core from 9,129 to 9,132 ft. This shows the variation in composition within the matrix perpendicular to the core length. Note the bright (high density) mineral in the matrix.

3.3.2 Micro CT Scanning

Detailed micro-CT scans of mm-scale sub-core sections were performed at NETL. The micro-CT scanner was used to obtain higher resolution images with voxel resolutions between 0.7637 and 4.0298 μm^3 and capture the details of internal features clearly, e.g., fracture connectivity, crosscutting relationships, and mineral morphology. A listing of the core sections scanned with the industrial CT scanner is shown in Table 3, followed by montages of images through the sides of these scans.

Table 3: Micro CT Scans of Sub-Cores (All Available on EDX)

Depth	File Name	Resolution (μm^3)
8,906.7	20210820 Robertson 8906.7 1-15H C2B6	3.9508
8,926.0	20210916 Robertson 8926.0 1-15H C2B13_4x	2.0526
8,926.0	20210916 Robertson 8926.0 1-15H C2B13_M70	3.9508
9,005.4	20210924 Roberson 1-15H C3B8 9005.4_10x	0.7637
9,005.4	20210924 Roberson 1-15H C3B8 9005.4_M70	4.0298
9,093.6	20210924 Roberson 1-15H C4B7 9093.6_10x	0.7637
9,093.6	20210924 Roberson 1-15H C4B7 9093.6_M70x	4.0298

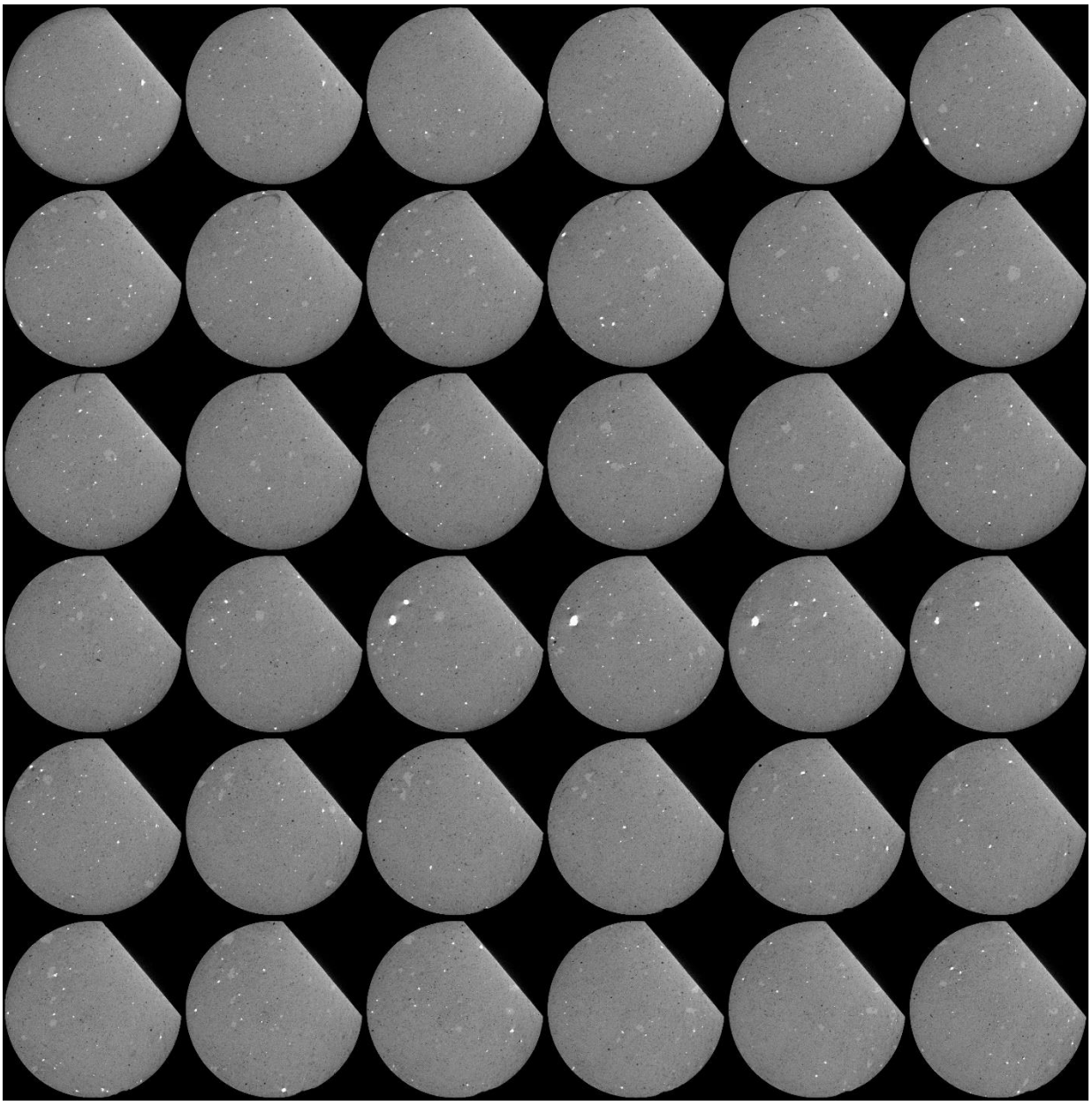

Figure 45: Micro CT montage of *"20210820 Robertson 8906.7 1-15H C2B6"* at 3.95µm^3.

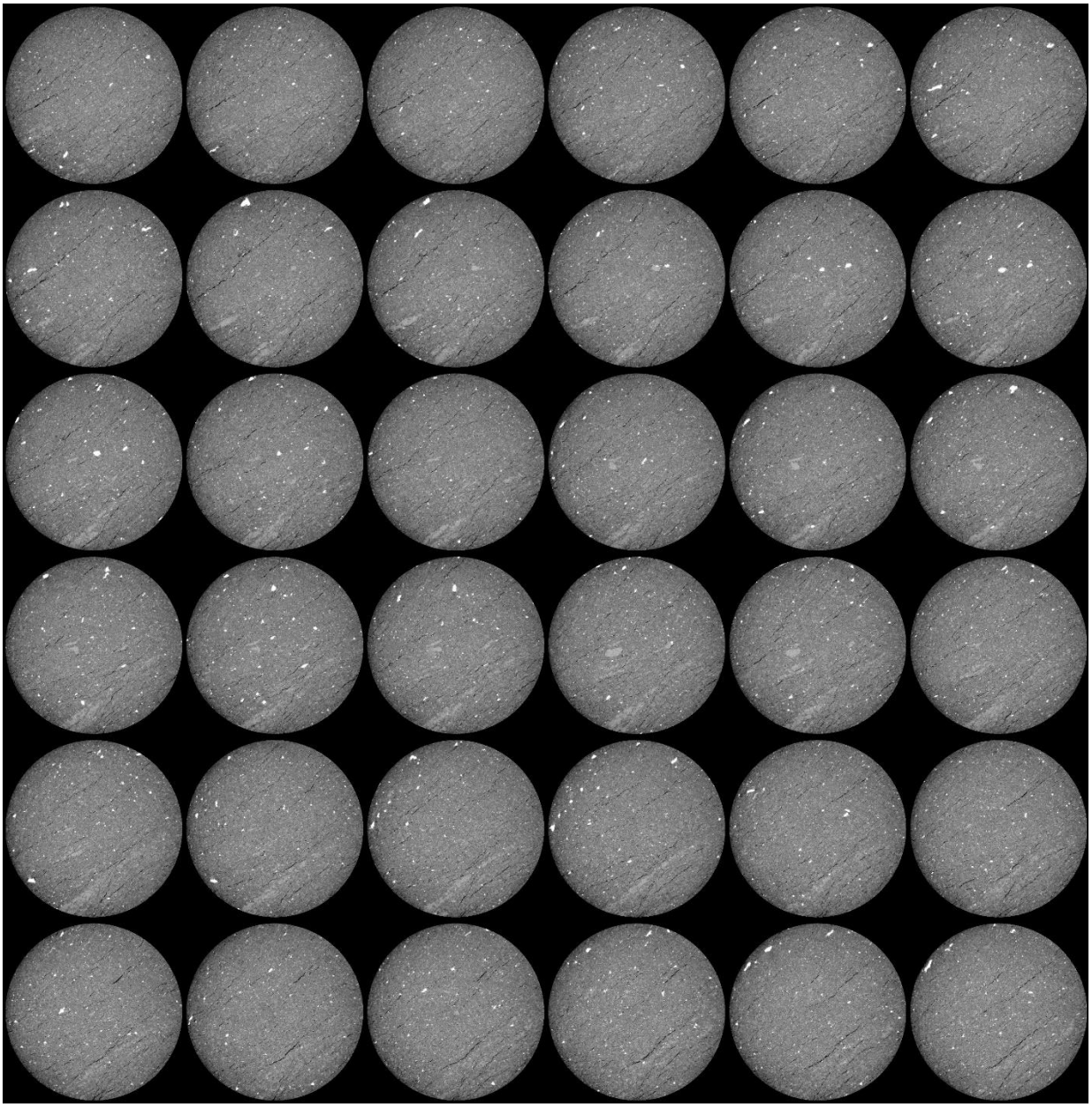

Figure 46: Micro CT montage of *"20210916 Robertson 8926.0 1-15H C2B13_M70"* at 3.95µm^3.

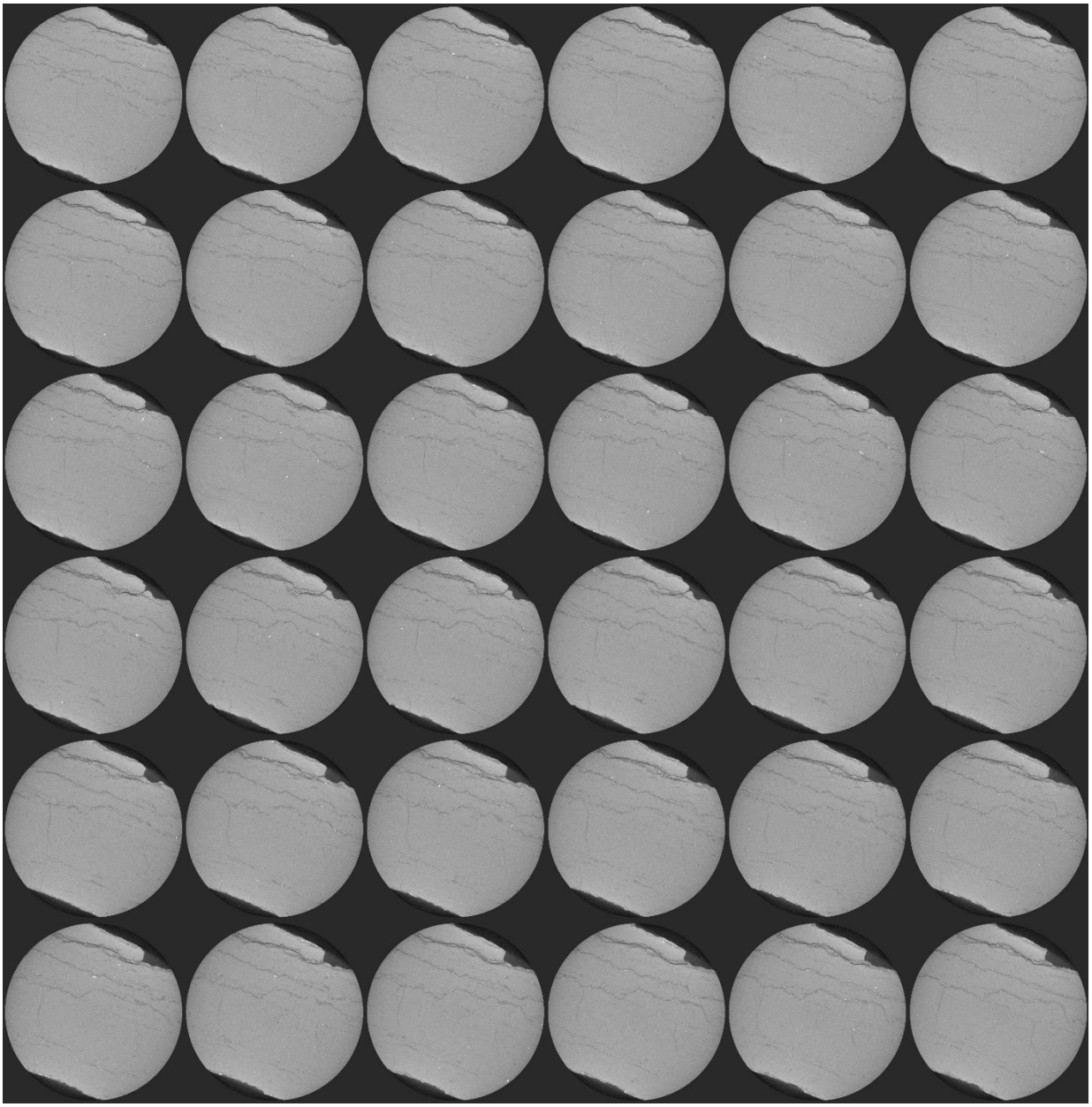

Figure 47: Micro CT montage of *"20210924 Roberson 1-15H C3B8 9005.4_M70"* at 4.03µm^3.

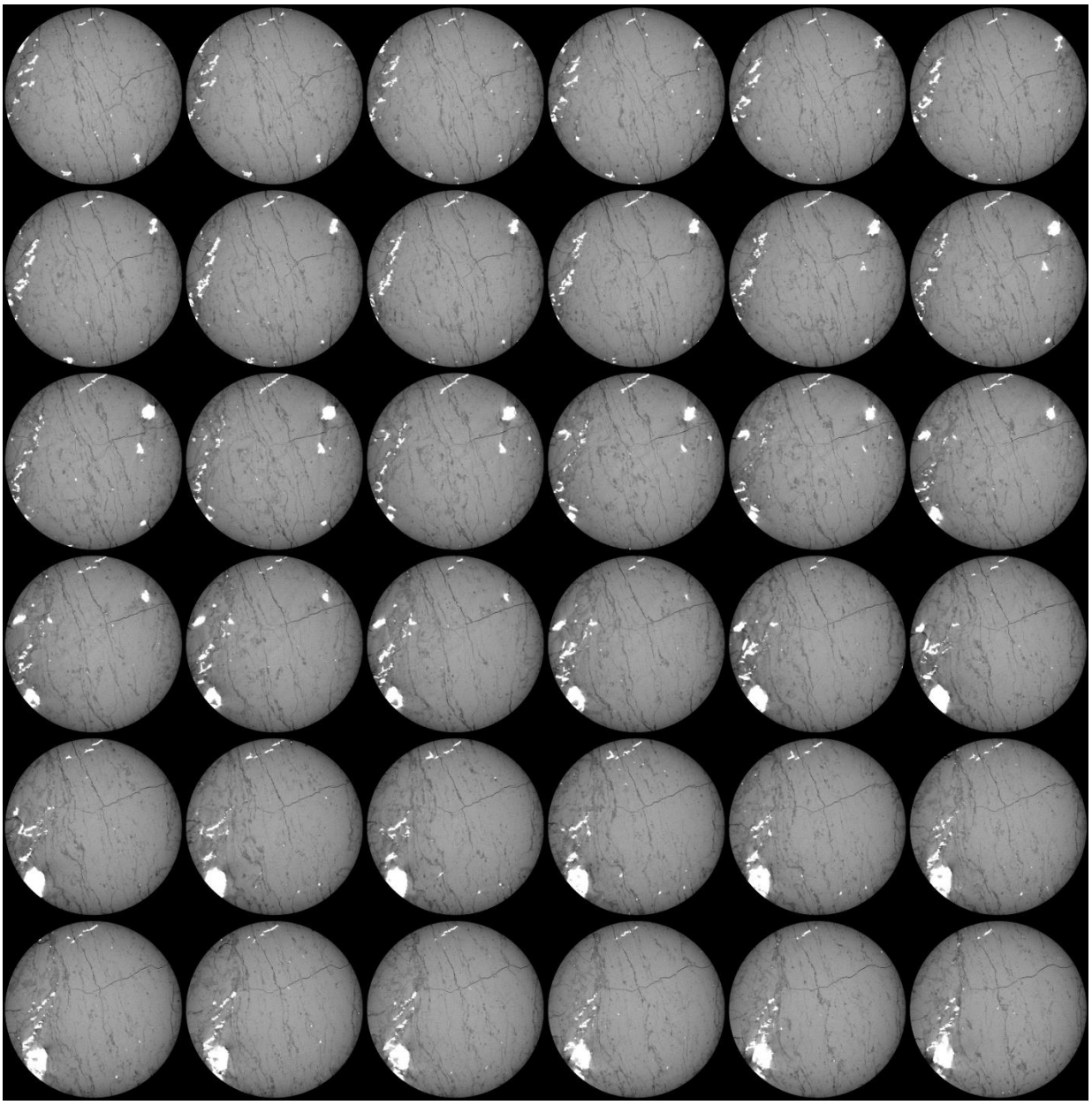

Figure 48: Micro CT montage of "20210924 Roberson 1-15H C4B7 9093.6_M70x" at 4.03µm^3.

3.4 DUAL ENERGY CT SCANNING

Dual energy CT scanning uses two sets of images, produced at different X-ray energies, to approximate the density (ρ_B) (Siddiqui and Khamees, 2004; Johnson, 2012). This technique relies on the use of several standards of known ρ_B to be scanned at the same energies as the specimen. These scans are performed at lower energies (<100 KeV) and higher energies (>100 KeV) to induce two types of photon interactions with the object (Figure 49). The lower energy scans induce photoelectric absorption, which occurs when the energy of the photon is completely absorbed by the object mass and causes ejection of an outer orbital electron (Figure 49a). The high energy scans induce Compton scattering, which causes a secondary emission of a lower energy photon due to incomplete absorption of the photon energy in addition to an electron ejection (Figure 49b)).

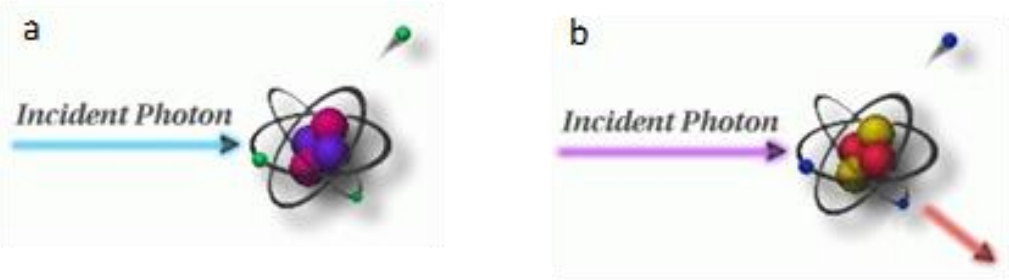

Figure 49: Photon interactions at varying energies. a) Photoelectric absorption, b) Compton scattering. Modified from Iowa State University Center for Nondestructive Evaluation (2021).

Medical grade CT scanners are typically calibrated to known standards, with the output being translated in CTN or Hounsfield Units (HU). Convention for HU defines air as -1,000 and water as 0. A linear transform of recorded HU values is performed to convert them into CTN. This study used CTN as it is the native export format for the instrument, but it is possible to use HU. Dual energy CT requires at least 3 calibration points and it is prudent to utilize standards that approximate the object or material of interest. Pure samples of aluminum, graphite, and sodium chloride were used as the calibration standards as they most closely approximate the rocks and minerals of interest (Table 4). Most materials denser than water or with higher atomic masses have a non-linear response to differing CT energies (Table 5).

Table 4: Dual Energy Calibration Standards, Bulk Density (gm/cm^3)

Material	ρ_B (g/cm^3)
Air	-0.001
Water	1
Graphite	2.3
Sodium Chloride	2.16
Aluminum	2.7

Table 5: Dual Energy Calibration Standards, HU and CTN for "Low" and "High" Energies

Material	HU		CTN	
	80 KeV	135 KeV	80 KeV	135 KeV
Air	-993	-994	31,775	31,774
Water	-3.56	-2.09	32,764	32,766
Graphite	381	437	33,149	33,205
Sodium Chloride	1,846	1,237	34,614	34,005
Aluminum	2,683	2,025	35,451	34,793

Dual energy CT utilizes these differences to calibrate to the X-ray spectra. Two equations with 3 unknowns each are utilized to find ρ_B (Siddiqui and Khamees, 2004):

$$\rho_B = mCTN_{low} + pCTN_{high} + q$$

$$Z_{eff} = \sqrt[3.6]{\frac{(rCTN_{low} + sCTN_{high} + t)}{(0.9342 * \rho_B + 0.1759)}}$$

Where [m, p, and q] and [r, s, and t] are unknown coefficients that can be solved by setting up a system of equations with four 3x3 determinants. The CTN is obtained from the CT scans for each of the homogenous calibration standards.

In this study, the high and low energy image stacks were loaded into Python as arrays. A 3D Gaussian blur filter with a sigma of 2 was used to reduce noise in the images. The scipy.solv module of Python was then employed to solve for the coefficients based on the calibration CTN values. The ρ_B was solved for each pixel in the 3D volume and saved as two new separate image stacks. The Z_{eff} was solved for at each pixel as well, and the data is available on the EDX data page.

3.5 COMPILED CORE LOG

The compiled core logs were scaled to fit on a single page for rapid review of the combined data from the medical CT scans and MSCL readings (Figure 50). The logs display data from the major elements, elemental ratios, elemental proxies, CT image, and dual energy density. Features that can be derived from these combined analyses include determination of mineral locations, such as pyrite, from magnetic susceptibility and using the XRF to inform geochemical composition and mineral form.

Data from the MSCL was filtered to remove areas of fractures and missing core, P-wave velocity was limited to values greater than 330 m/s, gamma density (and dual energy density) where limited to values greater than 1.5 g/cm^3, and Zeff was limited to values greater than 12.

The elemental results from the XRF were limited to major elements (Ca, Si, Al, Fe) and elemental proxies related to redox potential (Cr, Ni, and V), biogenic production (P and V*), skeletal influx/carbonate potential (Ca and Mn), detrital influence (Zr, Ti, Al, Si), and chalcophiles (Pb, S, Fe).

Trends in elemental ratios can provide insight into mineral composition, oxidation state, and depositional setting. Examples include: Ca/Si, which provides information on relative abundance of calcium carbonates versus silicates; Mn/Fe, provides information on oxidation, where a decrease in the ratio is related to zones of anoxic/euxinic conditions and an increase is related to zones of dysoxic/oxic conditions; S/Fe, which provides information on the abundance of pyrite (and other iron sulfates) versus Fe oxide minerals; Fe/Al, which provides information about the degree of pyritization in shales; Ti/Al, which provides information about terrigenous input; and Si/Al, which provides information on the abundance of illite and micas versus other clays. Magnetic susceptibility can test for iron sulfides (reducing) or oxidized Fe and sulfate. The elemental proxy log also includes an XRF “mineralogy” with Al, representing clays; Ca, representing calcite; and Si, representing only quartz, although there is some Si contribution to the clays. Pyrite (reduced) should have low magnetic susceptibility, and Fe oxide or hydroxide should have high magnetic susceptibility. These broad trends can quickly give information on large suites of core and direct more focused research. The logs are presented in the following Figure 50. Missing data on the logs are due to interruptions in the core logging equipment.

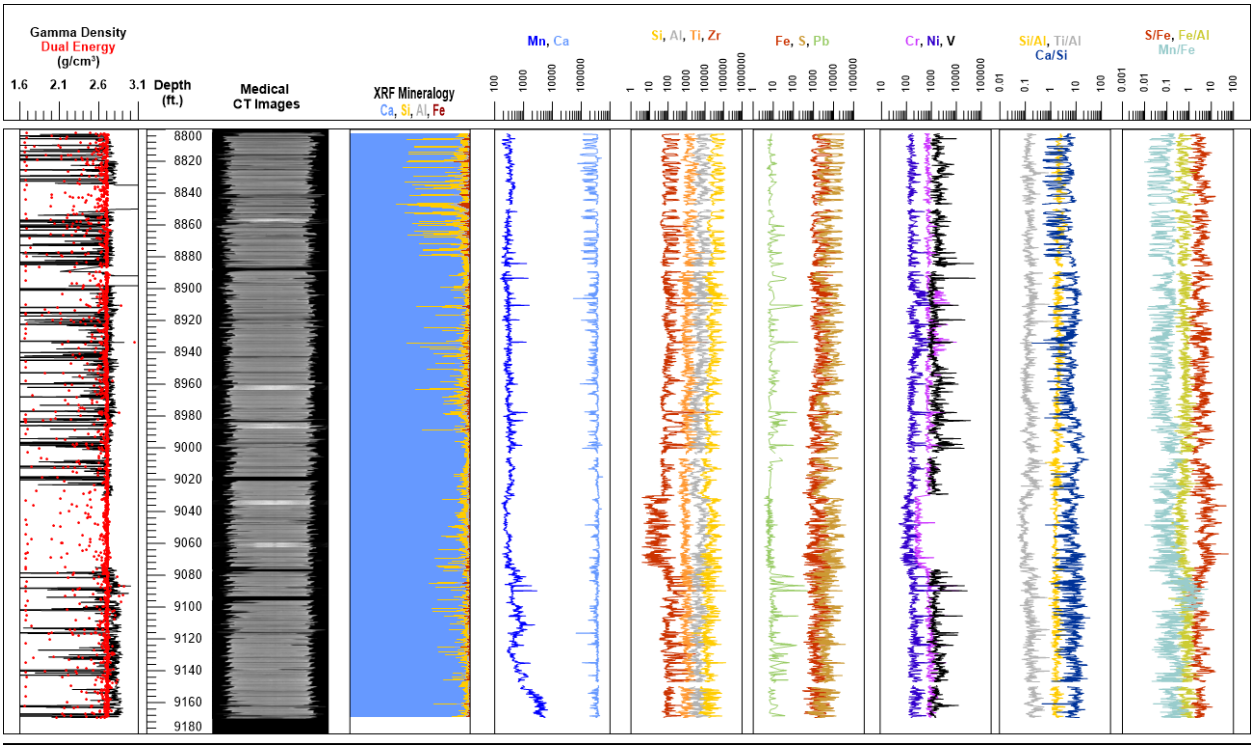

Figure 50: Compiled core log for Roberson 18-19 with major elements and elemental ratios, from 8,802 to 9,169.6 ft.

4. DISCUSSION

The measurements of the magnetic susceptibility, P-wave velocity, XRF, and CT analysis provide a unique look into of the internal structure of the core and macroscopic changes in lithology. These techniques:

- Are non-destructive
- Coarse resolution CT measurements allows for well-scale correlation, identification of lithological changes, and sedimentary structures, e.g., stylolites; while fine resolution aids in morphological description of minerals and fractures.
- When performed in parallel give insight into the core beyond what one individual technique can provide, e.g., at depth 9,093.6 ft the medical CT image has a white zone of high density, which the correlating micro-CT montage display in more detail as white nodules and fractures, while the XRF log of S/Fe ratio indicate relatively high (3.6) pyrite abundance compared to relatively low pyrite abundance (1.2 and 1.5) directly above and below, respectively.
- Can be used to identify zones of interest for detailed analysis, experimentation, and quantification
- Provide a detailed digital record of the core, before any destructive testing or further degradation, that is accessible and can be referenced for future studies.

This page intentionally left blank.

5. REFERENCES

Ahr, W. M. The carbonate ramp – an alternative to the shelf model. *Gulf Coast Association of Geological Societies Transactions* **1973,** *23*, 221–225.

Arkansas Geological Survey. https://www.geology.arkansas.gov/maps-and-data/well-cuttings-core-inventory-well-logs.html (accessed July 5, 2022).

Bishop, W. F. Petrology of upper Smackover limestone in North Haynesville Field, Clairborne Parish, Louisiana. *American Association of Petroleum Geologists* Bulletin **1986,** *52*, 92–128.

Bruce, W. A. A Study of the Smackover Limestone Formation and the Reservoir Behavior of its Oil and Condensate Pools. *Trans. Am. Inst. Min. and Met. Eng., Petrol. Devel. And Technol.* **1944,** *155*, 88–120.

Crandall, D.; Moore, J.; Rodriguez, R.; Gill, M.; Soeder, D.; McIntyre, D.; Brown, S. *Characterization of Martinsburg Formation using Computed Tomography and Geophysical Logging Techniques*; NETL-TRS-4-2017; NETL Technical Report Series; U.S. Department of Energy, National Energy Technology Laboratory: Morgantown, WV, 2017; p. 68.

Dickinson, K. A. *Upper Jurassic Stratigraphy of some parts of Texas, Louisiana, and Arkansas*; Geological Survey Professional Paper 594-E; 1968.

Geotek Ltd. Geotek Multi-Sensor Core Logger Flyer, Daventry, UK, 2009. http://www.geotek.co.uk/sites/default/files/MSCLOverview.pdf

Geotek Ltd. Multi-Sensor Core Logger Manual; Version 05-10; Published by Geotek, 3 Faraday Close, Daventry, Northamptonshire NN11 8RD, 2010. www.geotek.co.uk

Handford, C. R.; Baria, L. R. Geometry and seismic geomorphology of carbonate shoreface clinoforms, Jurassic Smackover Formation, north Louisiana: In *Seismic Geomorphology: Application to Hydrocarbon Exploration and Production*; Davies, R. J., Posamentier, H. W., Wood, L. J. and Cartwright, J. A., Eds.; Geological Society, London, Special Publications, 2007; Vol. 277, 171–185

Hunts, C.; Moskowitz, B.; Banerjee, S. *Magnetic Properties of Rocks and Minerals;* Rock Physics and Phase Relations: A Handbook of Physical Constants; 1995; 189–204.

Iowa State University Center for Nondestructive Evaluation, Ames, IA, 2021. https://www.nde-ed.org/Physics/X-Ray/attenuation.xhtml (accessed July 2021).

Johnson, T. R. C. Dual-Energy CT: General Principles. *American Journal of Roentgenology* **2012,** *199*(5_supplement), S3–S8. DOI: 10.2214/AJR.12.9116.

Mancini, E. A.; Aharon, P.; Goddard, D. A.; Barnaby, R. *Basin Analysis and Petroleum System Characterization and Modelling, Interior Salt Basins, Central and Eastern Gulf of Mexico*; U.S. Department of Energy, 2006.

Moore, C. H.; Druckman, Y. Burial diagenesis and porosity evolution, Late Jurassic Smackover, Arkansas and Louisiana. *The American Association of Petroleum Geologists* **1981,** 597–628.

Riggs, C. H. *Petroleum-Engineering Study of Atlanta Oil Field, Columbia County, Ark.;* U.S. Department of the Interior, Bureau of Mines, 1949, p.104.

Salvador, A. Late Triassic-Jurassic paleogeography and origin of Gulf of Mexico basin. *AAPG Bulletin* **1987,** *71*, 419–451.

Salvador, A. Origin and Development of the Gulf of Mexico Basin, in *The Gulf of Mexico Basin, The Geology of North America*; Salvador, A., Ed.; Geological Society of America: Boulder, CO, 1991b; v. J; p. 389–444.

Salvador, A. Triassic-Jurassic, in *The Gulf of Mexico Basin, The Geology of North America*; Geological Society of America: Boulder, CO, 1991a; v. J, p 131–180.

Sawyer, D. S.; Buffler, R. T.; Pilger, Jr., R. H. The crust under the Gulf of Mexico basin, in *The Gulf of Mexico Basin, The Geology of North America*; Salvador, A., Ed.; Geological Society of America: Boulder, CO, 1991; v. J, p. 53–72.

Schneider, C. A.; Rasband, W. S.; Eliceiri, K. W. NIH Image to ImageJ: 25 years of image analysis. *Nature Methods* **2012,** *9*, 671–675.

Siddiqui, S.; Khamees, A. A. Dual-Energy CT-Scanning Applications in Rock Characterization. *Society of Petroleum Engineers* **2004**. DOI:10.2118/90520-MS.

Brian Anderson
Director
National Energy Technology Laboratory
U.S. Department of Energy

David Alleman
Associate Director
Office of Research & Development
(FE-32)
U.S. Department of Energy

John Wimer
Acting Chief Research Officer
Science & Technology Strategic Plans
& Programs
National Energy Technology Laboratory
U.S. Department of Energy

Bryan Morreale
Associate Laboratory Director for
Research & Innovation
Research & Innovation Center
National Energy Technology Laboratory
U.S. Department of Energy

NETL Technical Report Series